This is to certify that the

thesis entitled

HIGH PRESSURE FUEL INJECTION STUDIES
IN A MOTORED ROTARY ENGINE ASSEMBLY

presented by

Todd B. Morita

has been accepted towards fulfillment
of the requirements for

Masters degree in Mechanical Engineering

Craig W. Somerton
Major professor

Date 02/22/91

HIGH PRESSURE FUEL INJECTION STUDIES IN A MOTORED ROTARY ENGINE ASSEMBLY

By

Todd B. Morita

A THESIS

Submitted to
Michigan State University
in partial fulfillment of requirements
for the degree of

MASTERS OF SCIENCE

Department of Mechanical Engineering

1991

ABSTRACT

HIGH PRESSURE FUEL INJECTION STUDIES IN A MOTORED ROTARY ENGINE ASSEMBLY

By

Todd B. Morita

A high speed flow visualization technique was utilized to study fuel spray development and the fuel-air mixing process in a direct fuel injection motored rotary engine assembly. Kerosene fuel was injected through a single hole nozzle at an angle of 60° from the horizontal axis into the combustion chamber. The nozzle was installed in a Servojet fuel injection system that was mounted in the central housing of a rotary engine. A 40 watt copper vapor laser was synchronized with a high speed rotating prism camera to expose motion picture films at 5000 frames per second (fps). The fuel spray structure was studied at injection pressures of 44 and 70 MPa, and at nominal injection durations of 1.2 and 2.8 ms. The engine shaft speed was 2000 rpm. A sequence of successive frames was selected from high speed films and used to analyze the fuel spray characteristics. The flow field and rotor motion which had contributing effects on the fuel spray behavior were also considered. The spray tip velocities and penetration distances for the fuel spray were quantified by analyzing the high speed films and were found to be significantly influenced by the injection pressure. The penetration distances from the high speed films were also compared to analytical expressions developed for high pressure fuel injection. Blowby past the apex seals is also briefly discussed. Finally, the mixing characteristics within the compression pocket were also observed in this thesis.

ACKNOWLEDGMENTS

At this point, I would like to express my gratitude and thanks to several people whose guidance was extremely important to this work. First, I would like to thank my advisor Dr. C. Somerton for his technical assistance and helpful suggestion that directed this research to its culmination; to Dr. H. Schock and Dr. E. Scott, the other committee members, for their invaluable time and supportive comments. I must also acknowledge Dr. F. Hamady, whose expertise in the flow visualization techniques made this work possible. I give thanks to my co-workers and peers for making my time spent at the MSU Engine Research Laboratory enjoyable. I must also express my thanks to my parents Marv and Estelle Morita for their loving support during my studies.

My last expression of thanks must be directed toward NASA Lewis Research Center for their support of this project.

TABLE OF CONTENTS

LIST OF TABLES

LIST OF FIGURES

LIST OF SYMBOLS

D - spray orifice diameter (m)

D' - spray orifice diameter in analytical spray cone angle calculations (mm)

ΔP - difference between injection pressure and combustion chamber pressure (MPa)

ΔP^1 - scenario 1 differential pressure term for analytical expressions (MPa)

ΔP^2 - scenario 2 differential pressure term for analytical expressions (MPa)

ΔP^3 - scenario 3 differential pressure term for analytical expressions (MPa)

$\Delta P'$ - difference between injection pressure and combustion chamber pressure (Pa)

S - penetration distance (mm)

S_1 - penetration distance used in explaining measuring techniques (mm)

S_2 - penetration distance used in explaining measuring techniques (mm)

t - time (s)

t_b - break-up length time (s)

T_a - air temperature at injection (K)

ρ_a - density of air (kg/m^3)

ρ_l - density of liquid fuel (kg/m^3)

μ_a - dynamic viscosity of air ($N\ s/m^2$)

θ - Jet Mixing spray cone angle in degrees

θ' - Hiroyasu and Kadota spray cone angle in radians

CHAPTER 1

INTRODUCTION

1.1 Problem Statement

The rotary combustion engine (RCE) just as other types of power plants (both traditional and non-traditional), are evaluated based upon their ability to meet industry standards and society requirements. Before the oil crisis of the early 1970's, the rotary engine was hailed as the new automotive engine of the future. The ability of the engine to produce smooth power at higher operating speeds along with its compact size made it very attractive to the automotive industry. To realize the potential of the rotary engine, the proponents of the engine understood that some of the inherent problems associated with the design would have to be corrected. In particular, the fuel consumption and emissions of the Wankel design needed to be improved, so that a rotor based power plant would be more acceptable to the domestic auto market. However, before these improvements could be realized, the oil crisis of 1973 and higher emission standards effectively ended the rotary engine research to which many of the domestic and foreign auto makers had earlier committed.

It is recognized that the performance of the RCE lies somewhere between the piston reciprocating engine and the small gas turbine. The RCE has a larger specific fuel consumption rate than that of a piston engine. However, the RCE fuel consumption is significantly less than the single small gas turbine engine. One of the most attractive characteristics of the RCE is its ability to consistently maintain its power density while using a variety of fuels.

Though the RCE has lost much of its appeal in the automotive industry (excluding Mazda), its potential to drive light aircraft has not been overlooked. The stratified rotary engine (SCRE) has received considerable attention in recent years as a means to develop more efficient power from the rotary design. Some applications include the possible replacement of large electric motors as well as an auxiliary power unit for large aircraft.

Economic factors also play an important role in the development of the rotary engine. It has been demonstrated by Deere & Co. that the SCRE can develop the predicted power density of four break horsepower per cubic inch of displacement

(4BHP/ci) [1]. It has been estimated by Hamady et al. [2] that a thermal efficiency increase of 25% is needed before the SCRE could be successfully introduced commercially to replace current power sources. A reasonable starting point to increase thermal efficiency of an internal combustion engine is to study the combustion process. More specifically, an enhancement of the fuel-air mixing through the use of high pressure fuel injection might provide exceptional results. In trying to better understand the characteristics of fuel injection process and its effects on the fuel-air mixing within the combustion chamber, it is hoped that this investigation will provide a sound foundation to further enhance the SCRE design.

A critical area in the development of the internal combustion engine involves appropriate control of the fuel distribution within the combustion chamber. An understanding of the fuel injection process is essential to evaluating and implementing strategies such as multi-stage injection or air blast assist atomization. Barber [3] defined the requirements of a fuel injector design as the following:

> "The performance requirement of the injector in conjunction with the rest of the system is to atomize the fuel finely and to distribute it throughout the combustion chamber so to ensure its complete combustion within the cycle time available, at all operating speeds and loads. This must be done without any deleterious effects such as dribble, secondary injections, hole choking or excessive smoke, hydrocarbon or NO emissions. There should be no premature failure due to stress, overheating or gas entering the nozzle during the closing phase."

The objective of the present study is to develop an understanding of the fuel-air mixing process in a direct injection rotary engine through the use of high speed film techniques and analysis. By better understanding the fuel-air mixing process, it is hoped that this study will assist in future designs of the direct injection rotary engine.

1.2 Literature Review

The advent of high speed, high pressure fuel injection systems has led to the consideration of a large number of injection options. Accompanying these options have been studies concerned with the performance of the injection system, both in and out of the engine. Out-of-engine studies are those studies that are conducted in quiescent engine situations or sometimes in ambient conditions. In engine studies indicate that actual

testing was conducted in the engine. The out of engine studies primarily focus on the development of visualization techniques and the evaluation of injector performance. Savey et al. [4] used stroboscopic flash photography to visualize the injection characteristics of the Servojet unit injector operating with water injection into quiescent air. The photographic evidence used in conjunction with dynamic laser attenuation measurements allowed the determination of spray penetration distance and spray cone angle. A shadow photographic technique was used by Kato et al. [5] for the analysis of non-evaporating fuel spray characteristics. The authors used a high pressure injection system which they developed in cooperation with Diesel Kiki Co., Ltd. They injected fuel into a high pressure, nitrogen-filled vessel and recorded fuel spray growth with a high speed camera. Spray droplet diameter and equivalence ratio were analyzed with shadow photographs. Katsura et al. [6] photographed the impingement of a diesel spray on a flat wall in a high pressure chamber with both transmitted and scattered light. The effect of ambient density was investigated and it was found that the growth of the spray radius decreases with increasing ambient density. Minami et al. [7] used high speed shadowed photography, holography and image analysis to evaluate the effect of injection pressure and injection rate upon the characteristics of non-evaporating fuel spray. The synchronization of a laser sheet with a high speed camera was first employed, in this application, by Hamady et al. [2]. These experiments were conducted by injecting kerosene into atmospheric air and several event to event variations in the injection process were observed that had not previously been noted.

Many of the out-of-engine studies used pressurized chambers with air flow to simulate in-engine situations. Hiroyasu and Nishida [8,9] used high speed Schlieren photographs to observe spray vaporization and analyze the structures of sprays in diesel engines. Varying quiescent chamber pressures and air densities, simultaneous droplet sizes and velocities of diesel fuel spray were studied using still photography by Koo et al. [10]. From the still photographs, frequency of surface waves on the liquid exiting from the nozzle were characterized. A repetitive micro-flash used in conjunction with a drum camera allowed Yoshikawa et al. [11] to observe spray behavior. They also conducted in-engine studies and utilized emission measurements to optimize the injection conditions. Heinze et al. [12] performed quantitative, ensemble averaged, two-dimensional fuel-air ratio maps in an injection jet by analyzing a series of single point Raman measurements. By injecting pure n-heptane into a special high pressure and temperature chamber, nearly 100,000 measurements were taken. From the data points a computer film was produced that illustrated the propagation of the inner spray, spray tip and their influence on the fuel-air mixing. Spatial and temporal characteristics of diesel

spray injected into ambient conditions through a multi-hole nozzle was studied by Arcoumanis et al. [13] using laser techniques. Results showed that the penetration and spray tip velocities increased as the frequency of injection increased, while at the same time, the injection volume was held constant.

Three studies are known to have performed visualization of the injection process within a firing engine. Werlberger et al. [14] used the endoscopic high speed combustion photography technique to study wall jet development, the role of swirl and the effect of pilot injection on mixture formation and combustion. Shimada et al. [15] used direct photography to study the non-vaporization part of the spray while at the same time, the vaporized part was detected by means of shadow photography. In conjunction with the fuel-air mixing, a high speed camera was utilized to study the actual combustion in a direct injection diesel cylinder. High speed shadowed methods were utilized to observe the combustion process in the cylinder in the study done by Minami [7].

Three-dimensional computational fluid dynamic simulations have been developed to characterize flow field, fuel-air mixing and combustion phenomena in the RCE. Chemically reactive flow, spray and combustion models were considered by Raju and Willis [16,17] in a stratified charge rotary engine. Preliminary results of pressure, temperature and velocity distributions as a function of crank angle were presented in addition to fuel concentration and droplet trajectories. Numerical analysis presented by Abraham et al. [18,19] of pressure measurements and fuel-air mixing contributed to specific design changes and recommendations to optimize fuel economy and fuel injector locations in the engine.

Using a two-dimensional numerical approach Shih et al. [20] have developed a grid generation technique to study the interaction of fuel injected into the combustion chamber with the flow field and the fuel-air mixing during compression stroke. Their results revealed valuable information on the flow patterns and the fuel-air mixing. Later their effort was extended to include three-dimensional calculations in Steinthorsson et al. [21] and Li et al. [22] by modifying the two dimensional code.

It is important to note that there have been no experimental studies concerned with the in-engine visualization of the fuel injection process within the rotary engine. In the present study, the laser sheet-high speed photography visualization technique of Hamady et al. [23] was employed. Three primary parameters affecting the injection process and subsequent fuel-air mixing have been identified: injection pressure, injection timing and injection angle. All three parameters are considered in the present work. The injection pressure is controlled by the rail pressure on the BKM Servojet Injection System. A Hall effect meter was used to set the injection timing with respect to the

crank shaft and rotor position. The injection angle is the angle between the injection jet and the axis of the injector assembly shown in Figure 1. Special nozzle tips have been manufactured to achieve injection angles of 60° ,45° and 30°. The 60° nozzle used in this study had a nozzle length to diameter ratio (L/D) of 4, as seen in Figure 1. This paper continues with a thorough description of the experimental apparatus and procedure.

The objectives for this study were to verify that high speed flow visualization techniques could be used to observe the injection event. Second, observable changes in the fuel injection characteristics when the operating parameters were varied was desired. Third, the feasibility of the angled injection used to direct the spray up into the compression chamber was to be determined. Finally, comparing experimental findings to quiescent and theoretical expressions was sought after. The listed objectives will be addressed in the flow visualization results. The study concludes with a summary and some recommendations for future research directions.

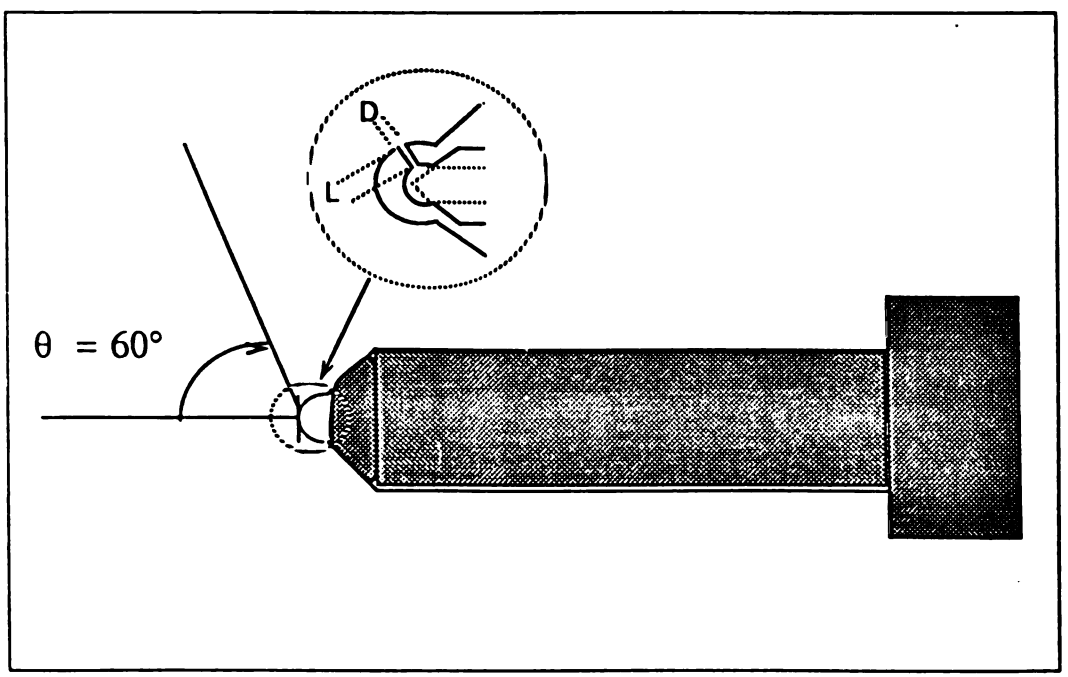

Figure 1 Injector nozzle showing angle of injection

CHAPTER 2

EXPERIMENTAL EQUIPMENT AND PROCEDURES

2.1 Experimental Equipment

In the following section, the experimental equipment used in this study will be presented. The fuel injection system as well as the rotary assembly and flow visualization system will be discussed in detail.

2.1.1 Fuel Injection System

The Servojet Fuel Injection System consists of four (4) basic elements:

1. SE-4D electronic controller
2. Hall Effect Sensory System
3. Electronically regulated hydraulic system
4. Electronic Unit Injectors

The SE-4D controller box provides the capability of operating the fuel injection system in the in-engine mode or bench test mode. The SE-4D allows for easy adjustment of the injection timing, solenoid energize time, engine speed or calibration frequency and rail pressure.

The operating mode for the fuel injection system is controlled by a variable switch on the SE-4D. When running bench tests or out of engine studies, the calibration mode is selected. Within this mode, the energize time (or the amount of time the injector solenoid is on), firing frequency and rail pressure can be manually adjusted. When firing the injector in a running engine, the load mode is selected. Under load mode, the firing frequency of the injector is determined by the crankshaft speed with all other parameters that were accessible under the calibration mode still remaining accessible. Figure 2 shows the SE-4D along with the adjustable parameter switches. In order to utilize the engine speed to fire the injector, a Hall Effect Sensory System (HESS) must be utilized.

The HESS is comprised of a Hall Effect Mask (HEM) and a Hall Sensor Pickup (HSP). The HEM rotates at crankshaft speed that utilizes one modified metal tab to give a rotor position reference. The HSP is positioned to allow the tab in the HEM to pass through its magnetic sensor. Once the metal tab passes through the HSP, an electrical

Figure 2 SE-4D control box for injection system

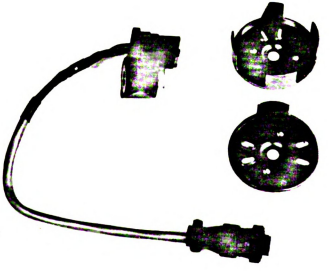

Figure 3 Hall effect system

pulse is created and sent to the SE-4D microprocessor. The signal is analyzed and the engine speed and injection firing rate is determined. Figure 3 shows the HEM and HSP before installation.

Through the hydraulic system, fuel is supplied to the injector and excessive fuel is bled off and returned to the fuel reservoir. Rail pressures are controlled by an electronic pressure regulator which includes a safety relief valve, accumulator and return check valve. Fuel delivery is controlled by the regulation of the rail pressure. It is the communication between the electronic controller and a solenoid valve which positions a spool to achieve a programmed or manually selected rail pressure which makes the regulation of the rail pressure possible.

Some of the vital components of the hydraulic system will now be discussed. The transfer pressure pump operates in a range of 10-20 psi, and it must be able to supply the maximum quantity of fuel utilized by the engine. The heat exchanger regulates the fuel temperature before it reaches the injector, and the rail pressure pump has a maximum operating pressure of 1500 psi. Figure 4 shows a simple schematic drawing of the Servojet Fuel Injection System.

The electronic unit injector consists of four elements:

1. Solenoid valve
2. Pressure intensifier
3. Accumulator
4. Nozzle tip

The first stage solenoid valve is an interface between the injector and electronic controller. When the solenoid is energized, a high pressure plunger in the fuel injector intensifier is actuated which supplies the required amount of fuel into the accumulator. The intensifier is capable of raising the effective pressure in the nozzle body to 15 times that of the rail pressure . When the solenoid is de-energized, the low pressure piston and high pressure plunger retract, causing a pressure differential on the needle valve. During the pressure imbalance, the needle is lifted which opens the nozzle tip orifice to the fuel stored in the accumulator. Injection will continue until such a time when the pressure difference between the accumulator and the needle valve closing pressure no longer exists or in other words, the pressure forces equilibrate. The needle valve closing pressure is predetermined by a spring force.

Special nozzle tips were manufactured by BKM Inc. for this study. Standard nozzle tip (tips that inject in a direction along the central axis) were modified to inject at

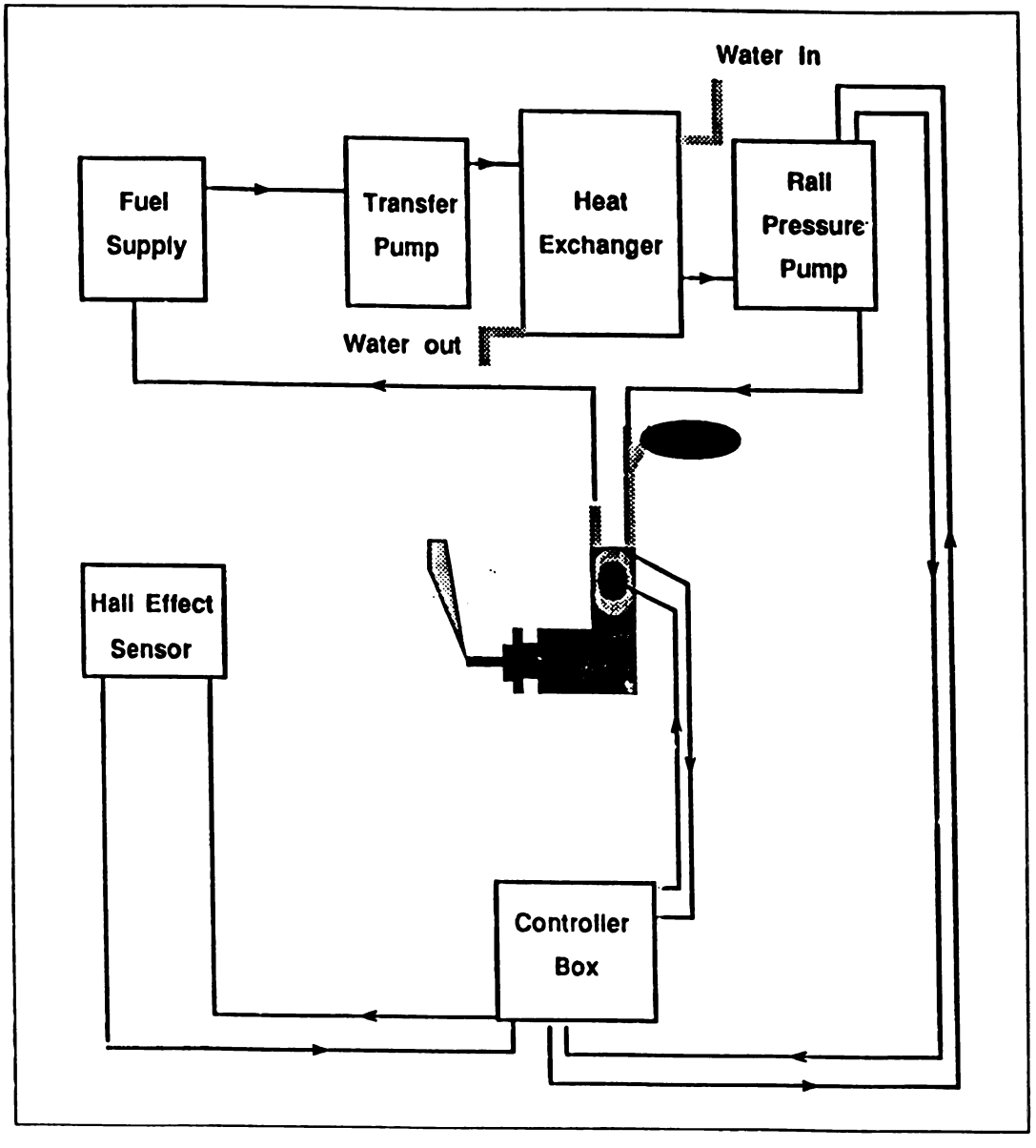

Figure 4 Fuel injection schematic

angles of 30°, 45° and 60° from the central axis of the injector. The injector orifice hole for all three nozzles has a diameter of 0.217 mm leading to a nozzle length to diameter ration (L/D) of 4. All three nozzle tips were tested under static conditions (the engine was not motored) to verify their feasibility in this study. From these results, only the 60° nozzle was utilized in this study. Further details of the verifications of the modified nozzles are discussed in the Experimental Procedures (Section 2.2).

2.1.2 Rotary Engine Assembly

The basic operation of the RCE is fundamentally different than any other internal combustion reciprocating engine. Power is transmitted to the crankshaft through torque which is produced by the eccentricity of the rotor as the rotor gear revolves around the stationary gear of the crankshaft. The position of these gears in the rotor engine can be seen in Figure 5. The rotary engine is characterized as a high power density engine. This attribute of the rotary engine is due to its unique method of operation. In the rotary engine, the intake, compression, combustion and exhaust cycles occur concurrently during the operation of the engine. The tricoidal shape of the engine housing along with the three-lobed rotor form three distinct chambers where these four

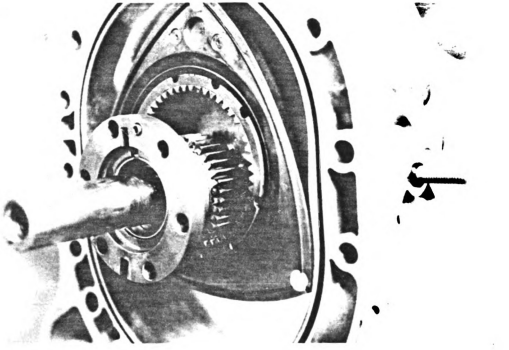

Figure 5 Walking gear for rotor assembly

cycles occur. From this configuration, the rotor engine is able to obtain three power strokes for every one revolution of the rotor.

The rotary engine used in this study was a single rotor peripherally ported custom fabricated assembly based on a Mazda 12A geometry [24]. Figure 6 shows the fuel injector and the mounting assembly used in the central housing at the modified upper spark plug hole. The schematic drawing in Figure 7 illustrates the necessary machining that was done to the inside housing wall to accommodate the angled injection of the nozzle. In Figure 8, a close up of the machined groove and injector tip can be seen. This assembly has been extensively updated during the past year. This change has resulted in a demonstrated increase in shaft speed up to 3400 rpm. Two major modifications have allowed for this significant increase in the engine operating speed.

One of the major modifications to the rotary assembly was a redesign of the lubrication system. Filtered oil is supplied by a gear pump to the rotor assembly at a regulated pressure range of 174-279 kPa (25-40 psi). Oil is then returned to a reservoir by means of a vacuum pump which is regulated by a flow control valve operating a 41 kPa (12" Hg). This is a closed system that originates and terminates at the oil reservoir. Two schematic diagrams of the lubrication system can be seen in Figure 9 and Figure 10.

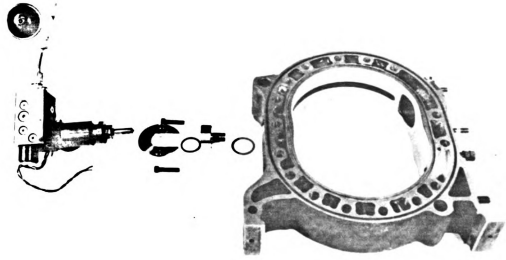

Figure 6 Fuel injector and mounting assembly for the central housing

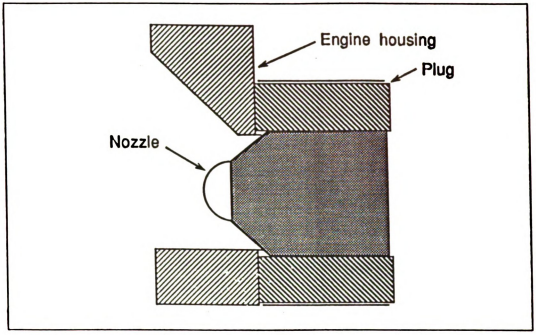

Figure 7 Nozzle seating in rotary engine housing

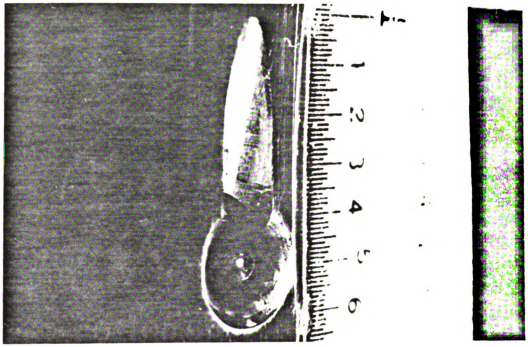

Figure 8 Fuel injector tip with modified engine housing wall

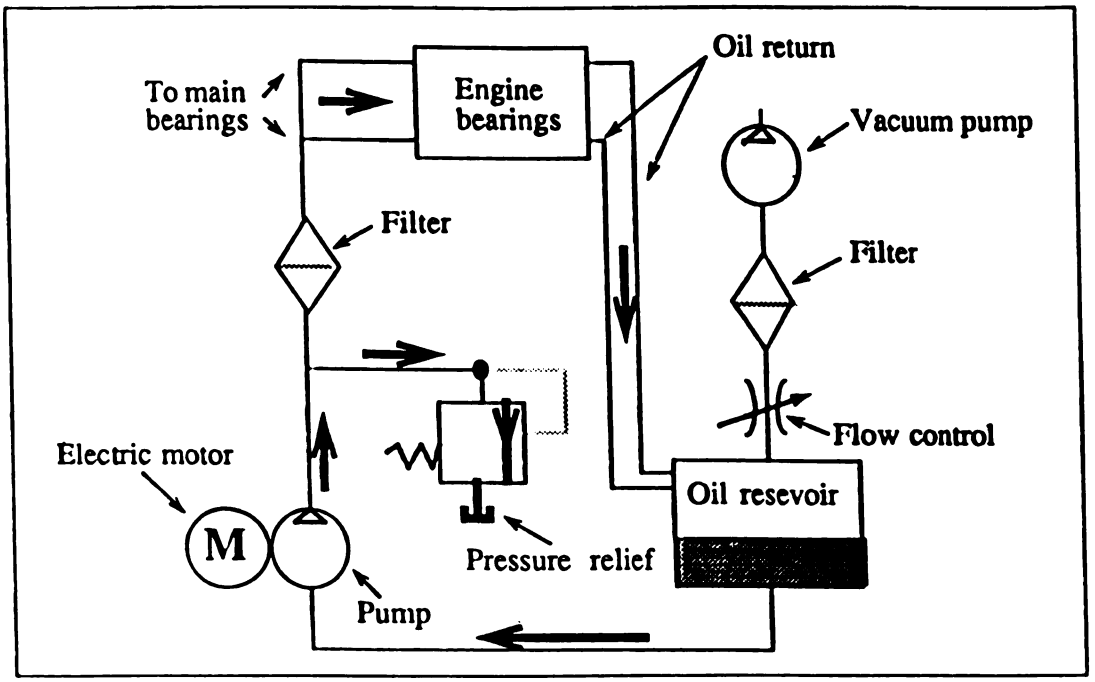

Figure 9 Schematic of lubrication system

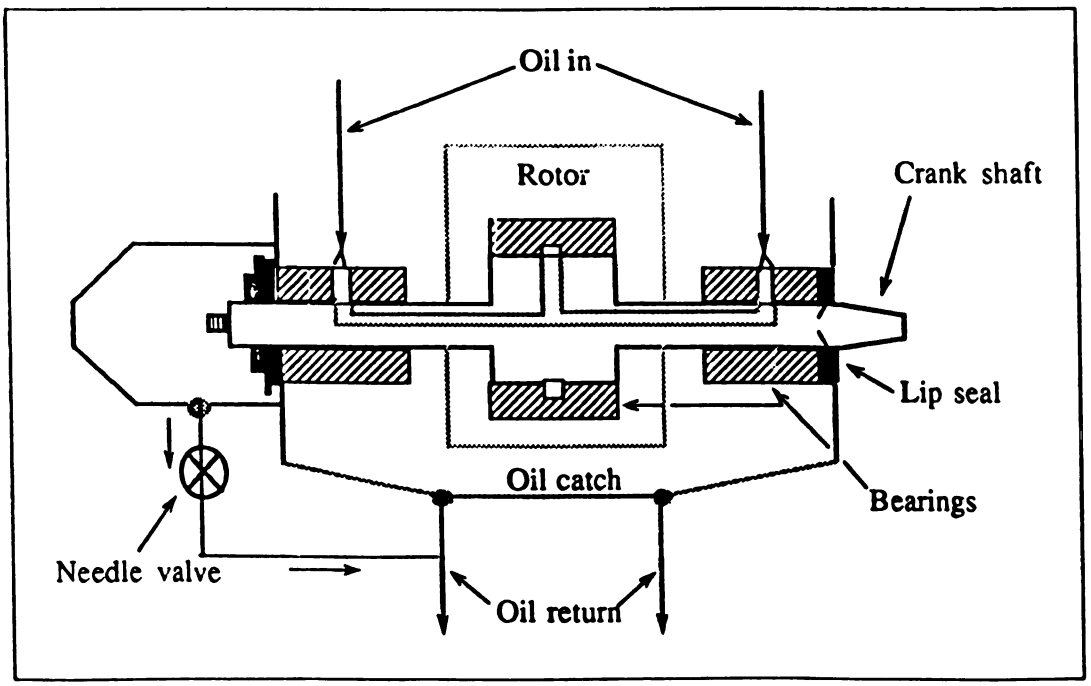

Figure 10 Lubrication of crankshaft and oil capture

The second major modification was to the side housings. A thin layer of chrome oxide was applied to the inside housing walls. The chrome oxide provides a smoother interface between the inside housing walls and the rotor side seals which allows the engine to run at higher speeds.

Production engine two-piece apex, side and oil seals were used in this work. More details on the seals and their installation will be discussed later in this section. Optical access was provided by custom fabricated sapphire windows that were mounted in the end housing. A plexiglass window was fitted in the top of the central housing chamber to allow for the access of the laser light needed for flow visualization. The plexiglass and sapphire windows are shown in Figure 11 and Figure 12.

One of the difficulties of the rotary engine is the sealing issue. In order for the engine to operate correctly, there must be minimal leakage between the three chambers. The chambers are isolated by using six side seals, three on each side of the rotor that ride in spring-loaded grooves sealing the area between the side housing and the side of the rotor. Apex seals are located in the apex of the three lobes. As in the case of the side seal, the apex seals also ride in spring-loaded groves. The purpose of these seals are to prevent interaction between the chambers at the rotor face and central housing along the lobe apex where the two rotor flanks meet. Finally, button seals, transition pieces that provide

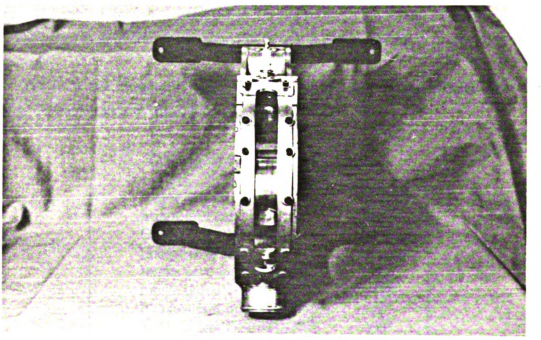

Figure 11 Laser access plexiglass window in the central housing

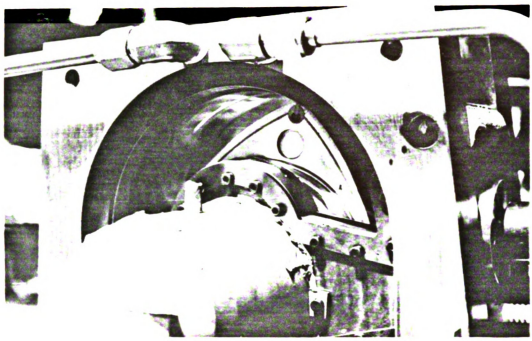

Figure 12 Sapphire side window for high speed camera access

sealing between the side seals and the apex seals, also ride in spring-loaded groves.

The engine was powered using a 7.5 kW (10.0 hp) constant torque electric motor. The motor is cooled by water delivered to the engine by nylon tubing attached to a water facet. The water is delivered from the nylon tubing to the engine by steel tubing as shown in Figure 13.

The RCE test rig used in this study was a peripherally ported Mazda 12A central housing. Characteristics of the engine are given in Table 1.

Table 1 Rotary engine characteristics

Major axis (y)	120 mm
Minor axis (x)	90 mm
Generating radius (R)	105 mm
Eccentricity (e)	15 mm
Intake port opening (IPO)	267°
Intake port closing (IPC)	350°
Exhaust port opening (EPO)	12°
Exhaust port closing (EPC)	66°
Engine speed	3400 rpm

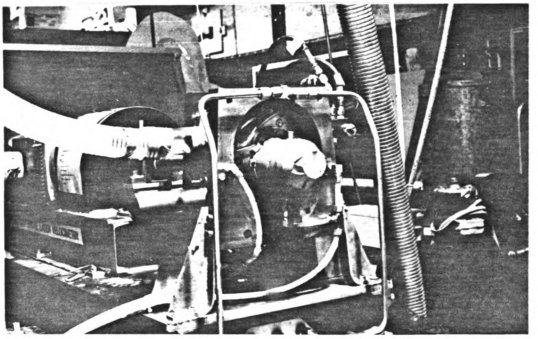

Figure 13 Nylon and steel water tubes to the motor

2.1.3 Flow Visualization System

The high speed flow visualization system used in this study is shown schematically in Figure 14. It consists of a 40 watt copper vapor laser (CVL) Model 451, a high speed camera Nac E-10/EE, mirrors and cylindrical lenses. The CVL is a gas discharge device of 40 watts of average output power. It emits 4000-6000 pulses per second (pps) with a pulse energy of 8 mJ in the green-yellow visible spectrum and a pulse duration of 30 ns. Figure 15 shows the CVL system used in this study. The camera is equipped with a trigger pulse generator and an optical pickup that triggered the CVL at 5 kHz for this study. The triggering system also made it possible to synchronize light pulses from the CVL with the Nac high speed camera.

2.2 Experimental Procedures

In this section the procedures utilized to perform this study will be discussed. The nozzle tip calibration, injection timing and flow visualization procedures will be introduced in the first three subsections. The techniques used to measure the penetration distance and spray cone angle are discussed in the next two subsections. Finally, in the

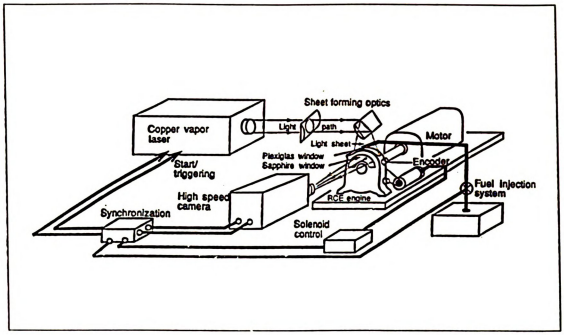

Figure 14 Schematic of flow visualization system

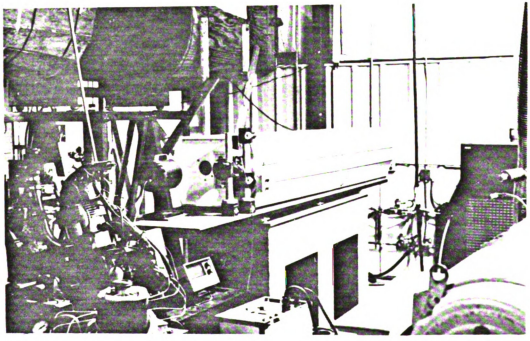

Figure 15 The copper vapor laser system used in study

last three subsections, the analytical expressions used to predict spray characteristics and the fuel-air mixing observations are discussed.

2.2.1 Nozzle Tip Calibrations

Before the special nozzle tips could be utilized in this study, three tests had to be conducted to verify that the nozzles were functioning properly. First, the nozzles had to be tested to verify that were capable of operating without extensive nozzle leakage (failure of the nozzle needle to seat properly in the sack chamber). Second, the angle of injection had to be examined for satisfactory orientation within the chamber. It was very important that the fuel spray be directed into the chamber with minimal obstruction (from the rotor and housing wall) over the largest possible crank angle range. Lastly, the fuel delivered per injection was important information needed for possible future reference of the fuel-air ratio characteristics of the test configuration. Information related to the standard 0.217 mm nozzle was available; however, since these angled nozzles were unique to this study, no calibration information was available on their delivery characteristics.

The first test captured on high speed 35 mm still film was the fuel injection event of the three nozzles. From these stills, it was possible to justify the nozzles performance in terms of a consistent fuel jet formation. Nozzles that leak tend to form inconsistent jet sprays and large fuel droplet which effects the performance of an engine. A 4 watt argon-ion laser manufactured by Coherent was utilized to provide lighting for a Nikon 35 mm camera. The laser was mounted on a rigid traverse table (model 9900-1). The laser and traverse table are actually part of a laser Doppler velocimeter system; however, only the illuminating power of the laser was of interest in this test. The fuel injection unit was secured to a bench stand. A series of mirrors were used to direct the laser beam to the bench stand where the laser beam was spread into a sheet of light by cylindrical glass rod. Figure 16 shows the experimental set up for the nozzle tip spray formation test. The camera was triggered externally by the SE-4D control box. Leads were taken from the SE-4D injector on-off switch and connected to the cameras remote adapter. When the injector on switch was engaged, the camera was automatically triggered to take a picture.

The second test captured the fuel jet spray within a modified rotary engine on high speed film. Special plexiglass side housings were machined which allowed the high speed camera to access the entire chamber where the fuel injection occurred. For this particular test, the engine was not motored, and the rotor was position to a crank angle of approximately 70° before top dead center (BTDC). A plexiglass window was installed in

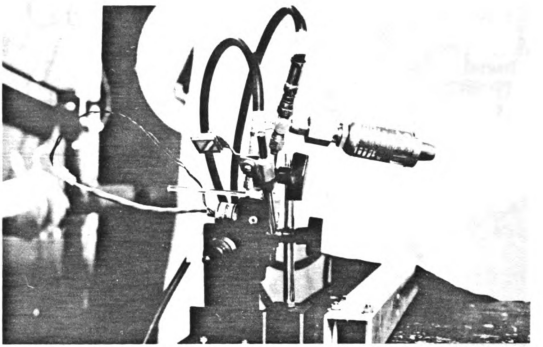

Figure 16 Bench stand set-up for the nozzle tip calibration tests

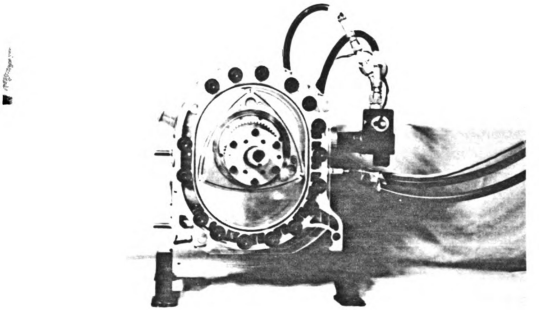

Figure 17 Fuel injector mounted into static engine

If you find the crush
leave the date and name →

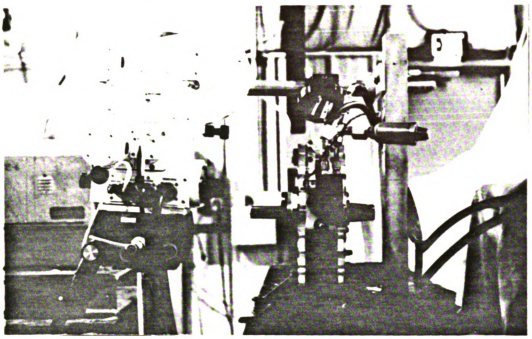

Figure 18 Positioning of high speed camera and reflecting mirror for static test

the central housing of the engine (much like the housing described in the earlier section) that allowed the laser beam to access the chamber for illumination purposes. The test engine along with the mounted fuel injector in the modified upper spark plug hole can be seen in Figure 17. The Nac E-10/EE high speed camera along with the 40 watt CVL were used to conduct this test and can be seen in Figure 18. The frame speed of the camera was 5000 fps and the CVL pulsed at 5 kHz. The triggering system made it possible to synchronize light pulses from the CVL to the camera. The operating mode on the SE-4D control box was set to the calibration mode. This calibration mode was chosen because the engine was not motored and the control of the firing frequency was desired. The firing frequency was set at 20 Hz, while the energized time and rail pressure parameters were set at 10 ms and 650 psi respectfully. After testing the 60° nozzle and reviewing the high speed film, further tests of the 45° and 30° were not pursued. The results and details of this test are discussed in a later section.

In the third test of the calibration procedure, an attempt was made to calculate the injectors performance using the 60° nozzle tip. A test matrix was constructed to guide this test. The rail pressure was varied using settings of 500, 700, 900, 1000, 1100, and 1200 psi. The frequency of injection was varied between 20, 30 and 50 Hz. Finally, the energize time was varied between 9, 10, 11, 12, 13 and 14 ms. These parameters were

chosen to mirror the test parameters of the BKM Inc [25]. calibration study of the standard 0.217 mm nozzle tip. Special nozzle adapters were constructed to allow easy collection of the injected fuel by a plastic container. The nozzle tip adapter was angled to 60° to minimize the restriction of fuel during the collection process. The fuel injector was mounted in the bench stand rotated 180° from the mounting position it assumes in the engine. The purpose of this mounting procedure was to ease the fuel gathering process by utilizing the gravitational force. Nylon tubing transferred the fuel from the adapter to the plastic container. The fuel injector and collection system can be seen in Figure 19.

An analytical balance, accurate to a 0.1 mg, was used to measure the plastic container and the collected fuel after each run and is shown in Figure 20. A total number of injections (nominally 2000) were weighed and recorded after each run. When the total weight of the collecting container and fuel approached the maximum rated weight limit (150 gms), the fuel was returned to the fuel reservoir. The plastic collecting bottle was then weighed again and the test was continued. The mass of fuel utilized per injection was simply calculated by taking the mass of fuel collected during the runs, and dividing it by the recorded number of injections.

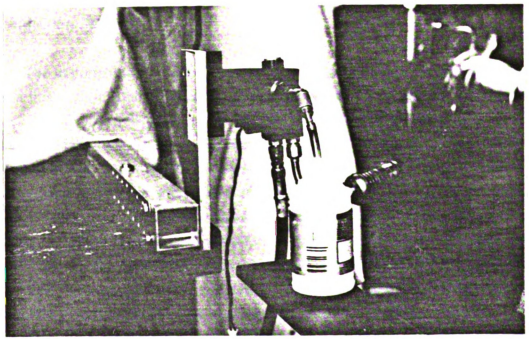

Figure 19 Calibration collecting bottle attached to injector nozzle

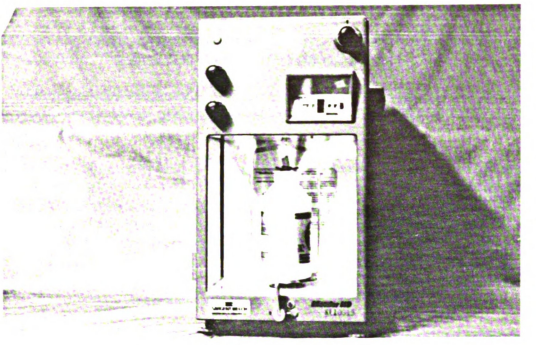

Figure 20 Analytical balance used in calibration test

2.2.2 Injection Timing

The importance of accurately setting the injection timing for the high speed films used in this study can not be overly emphasized. Proper timing settings were needed to ensure that a comprehensive study of the fuel injection characteristics could be completed. Many times in the engineering field, the techniques used to accomplish the work is new and unfamiliar to the researcher. The cost of engineering research is very expensive and progress is often measured against time. In this study, the production of one high speed film was an expensive process. Mistakes in the timing of the fuel injection could have resulted in films that were useless to this study. Injection events that occurred too early in the compression cycle might have yielded results in which the fuel did not have the proper means to vaporize. Firing the injector too late in the compression cycle might have resulted in a total blockage of the injection event by the rotor.

The timing procedure for synchronizing the injection event with the rotor position utilized both an angular encoder system and the injector Hall effect system. The following steps contain the procedure to setting up the injection timing.

1. The angular velocity is determined from the test rpm that will be used (typically in units of deg./ms).

2. From the BKM injector documentation [25], the injection delay time can be determined. The delay time is a function of the rail pressure.

3. Multiplying the injection delay time by the angular velocity found in step 1 will give the angle off-set (the angle adjustment to the rotor to account for the injection delay time).

4. One apex of the rotor should be aligned with the center window frame screw of the housing. This is 90° BTDC for the crankshaft position and is relatively easy to locate. For convenience, the apex position of TDC is referenced to 0°. The 90° reference angle assumes that the desired crank angle for injection is less than 90°. If for example the desired crank angle of injection is greater than 90°, then a larger crank angle for reference is suggested. The reasoning behind the crank angle reference selection becomes clear in later steps. Figure 21a-21b illustrate the 90° BTDC reference angle and the TDC position of the rotor respectively.

5. The rotor position during the injection process must be determined at or before this step. The rotor position is selected to the test specifications. To account for the injection delay time inherent to the mechanics of the fuel injector, the off-set angle is added to the crank angle of injection.

6. Once the final rotor position (rotor position for injection plus the off-set angle) is determined, subtract this from the 90° reference angle and advance the crankshaft toward TDC by this result.

7. Adjust the encoder shaft while at the same time monitoring the electronic output of the encoder with a volt meter. The leads of the volt meter must be attached to the encoder channel that outputs one pulse per revolution of the encoder. When the encoder responds with a pulse, the encoder shaft can then be coupled to the rotor crankshaft.

8. The final step is to synchronize the Hall effect censoring system to the encoder. The encoder and injector logic signal (on the SE-4D control box) are monitored with an oscilloscope. Note, the engine must be running at the same speed that the angular velocity was calculated at. The injector logic signal is a 5 volt square wave pulse transmitted to the injector actuator by the SE-4D. This 5 volt square wave corresponds to the energize time of the injector. The voltage spike from the encoder must line up with the trailing edge of the 5 volt square wave. To accomplish synchronization, the Hall effect mask is adjusted until both signals coincide. Figure 22 illustrates the correct orientation of both the encoder and injector logic signal for synchronization.

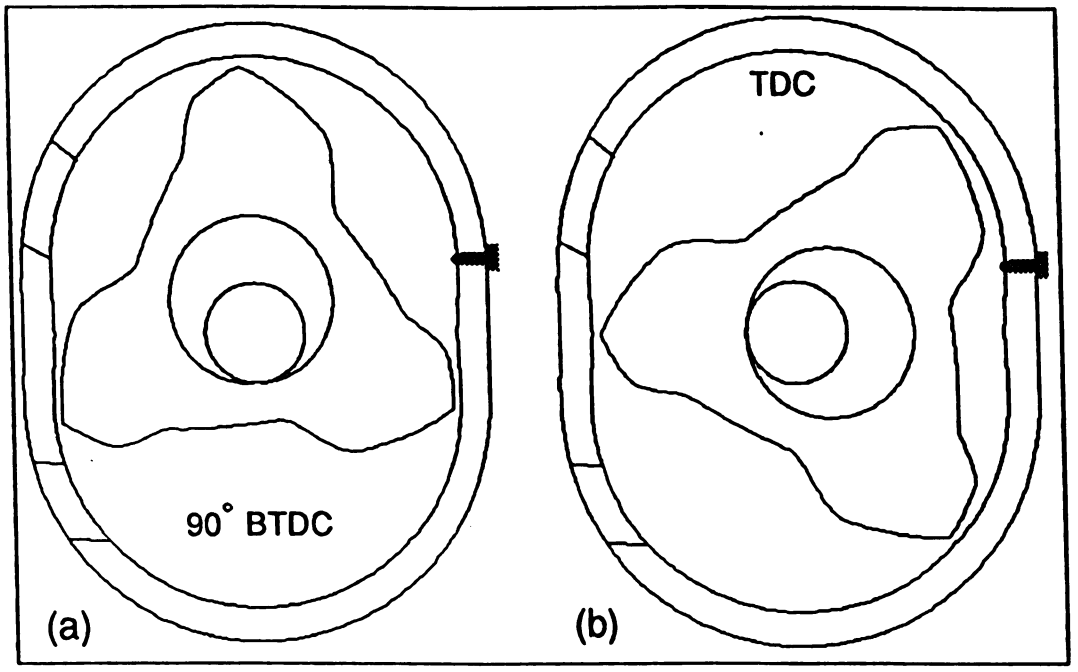

Figure 21 Rotor positions of 90° BTDC and TDC

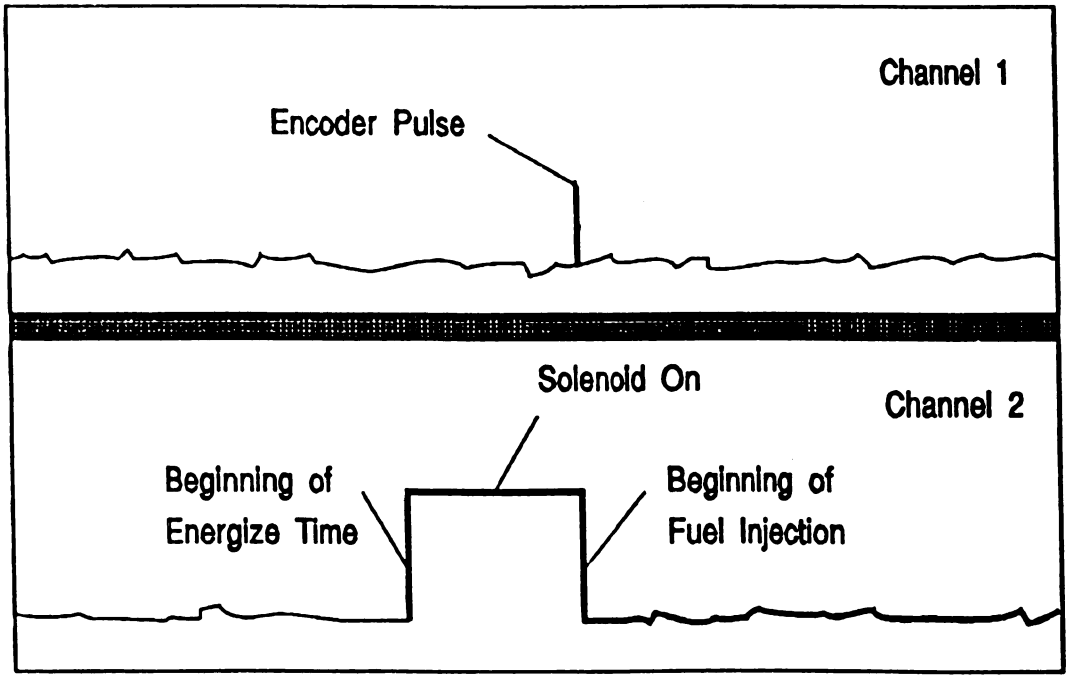

Figure 22 Oscilloscope output of encoder and hall effect meter for timing set-up

2.2.3 Flow Visualization

The CVL was configured to pulse at 5kHz with a power range of 35-38 watts. The pulse energy was 8 mJ in the green-yellow visible spectrum. The pulse duration was 30 ns. The Nac high speed camera was operated at 5000 frames per second (fps). Two hundred feet of high speed negative film was utilized for each case. Three different cases were considered for this study:

Case (i) Injection Pressure of 70 MPa (11,875 psi), Injection Timing of 70° BTDC

Case (ii) Injection Pressure of 44 MPa (6352 psi), Injection Timing of 65° BTDC

Case (iii) Injection Pressure of 44 MPa, Injection Timing of 55° BTDC

Each case was run with an engine speed of 2000 rpms. At this speed, the crank shaft and the rotor rotational velocities were approximately 12°/ms and 4°/ms. Figure 23 illustrates the rotor position at injection for each case.

The beam from the CVL was converted to a light sheet by cylindrical lenses and directed to the engine housing through a series of highly polished mirrors. Once the proper orientation of the laser beam was obtained, the synchronization between the

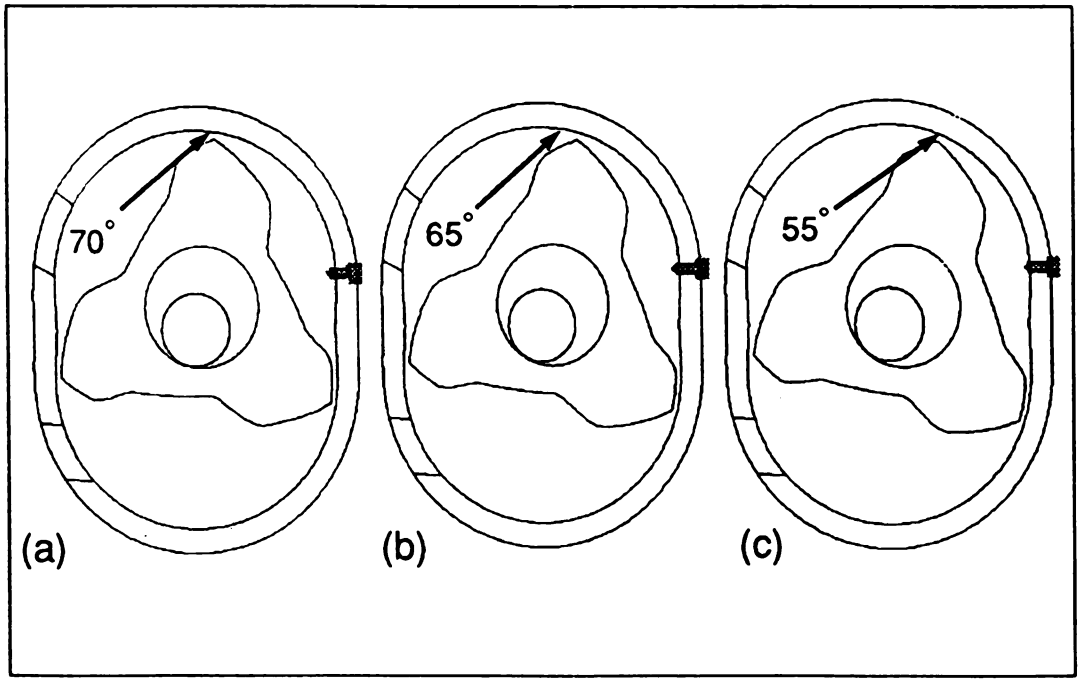

Figure 23 Rotor position at injection

high speed camera and the CVL was checked. By reflecting some of the laser light to the timing gears of the Nac camera while running at speed, the action of the timing tabs could be observed. If the tabs appeared to align with the timing mark during the synchronized test, then the synchronization between the camera and CVL system was successful. At this point, the Nac camera was positioned and focused to capture the injection events through the sapphire window. In Figure 24, the camera, engine housing and the final reflecting mirror are shown. After the injection system reached the proper rail pressure, the injector was fired while at the same time the camera was started.

2.2.4 Penetration Distance and Velocity Measurements

In processing the high speed films to obtain fuel spray penetration distances, a Nac DF-16C analysis projector along with a caliper measuring instrument accurate to 25 μm were utilized. In the films, there existed areas of well defined fuel distribution, surrounded by a cloud of scattered mist. The leading portion, or apex, of the well defined fuel distribution was used as the datum point. The distance from this point to the tip of

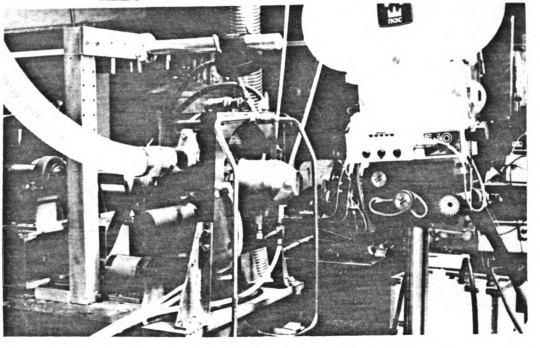

Figure 24 Camera positioned to capture injection events in motored engine

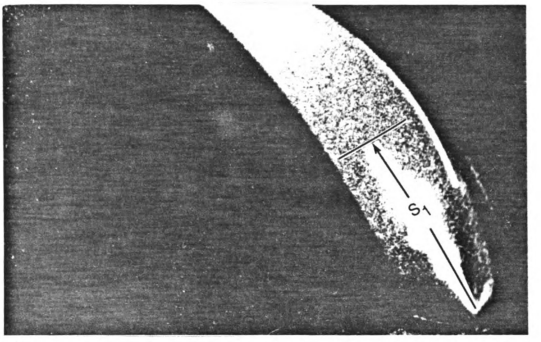

(a)

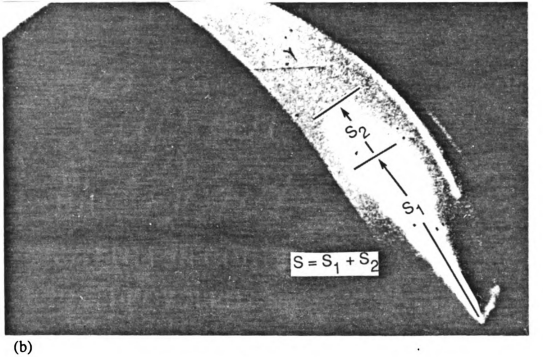

(b)

Figure 25 Penetration distance calculations

the injector was carefully measured using the caliper for each frame of the injection event. Velocity measurements were obtained directly from the penetration distances by simply dividing the penetration distance by the frame time. A film speed of 5000 fps corresponds to 0.2 ms per frame.The procedure for determining the penetration distance can be seen in Figure 25a-25b. Penetration distance and velocity plots verses time were constructed from the data obtained.

2.2.5 Spray Cone Angle Measurements

The spray cone angle measurements also utilized the Nac DF-16C analysis projector and caliper measuring device along with, a standard protractor. The spray cone angle is defined as the angle formed by two straight lines drawn from the injector tip to the outer edge of the spray distribution at a distance of 60xD', where D' is the spray orifice diameter [26]. In Figure 26, the technique of determining the spray cone angle from the high speed film is illustrated.

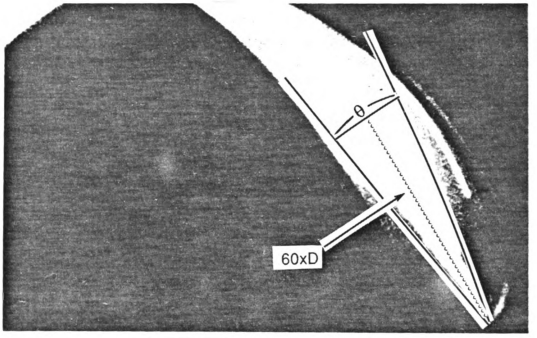

Figure 26 Measuring the spray cone angle

2.2.6 Analytical Penetration Distance Calculations

Two expressions were utilized in predicting the penetration distances of the injection spray for the three cases. The first expression used was the jet mixing theory [27]. The penetration distance were calculated using the following theoretical expression:

$$S = 3.01[(\Delta P / \rho_a)^{0.5} D * t]^{0.5} (295 / T_a)^{0.25} \qquad (1)$$

where ΔP is the difference between the injection pressure and chamber pressure. The density of the air in the chamber at injection is ρ_a. The injection orifice diameter is defined as D. Time is given by t. Finally, T_a is the air temperature inside the chamber at injection.

A previous fuel injection study by Hiroyasu and Arai [8] utilized non-visual means to quantify the structure of fuel sprays injected into quiescent air. Quiescent spray tip penetration distances were calculated using the following expression [8]:

For $0 < t < t_b$

$$S = 0.39(2\Delta P / \rho_l)^{0.5} * t \qquad (2)$$

For $t > t_b$

$$S = 2.95(\Delta P / \rho_a)^{0.25} (D * t)^{0.5} \qquad (3)$$

where t_b is defined as the break-up length time and is given by

$$t_b = 28.65[(\rho_l * D) / (\rho_a * \Delta P)^{0.5}] \qquad (4)$$

The parameter ρ_l is the density of the liquid fuel.

The theoretical and quiescent penetration distances were calculated and plotted verses time. Comparisons between the analytical calculations and the experimental results were conducted and are discussed later in the Results section of this paper.

2.2.7 Analytical Spray Angle Calculations

As in the case of the previous section, the analytical spray angle calculations utilized two different expressions. Theoretical spray angles were calculated [27] using the expression

$$\tan\theta = 0.13[1 + \rho_a / \rho_l] \qquad (5)$$

The second expression utilized to predict spray cone angles was developed by Hiroyasu and Kadota [28] and is given by

$$\theta' = 0.025[(\rho_a * \Delta P' * D^2 / \mu_a^2] \qquad (6)$$

where θ' is in radians and $\Delta P'$ is the difference between injection pressure and chamber pressure in units of MPa.

2.2.8 Fuel-Air Mixing Observations

An attempt to quantify the fuel-air mixing after the termination of the fuel injection event within the combustion chamber was made for all three high speed films. The ultimate goal in this procedure was to obtain some insight on how the fuel-air mixture behaved during the compression process once the injection event had ceased. The compression chamber was segmented into 'areas' of observation to make the process easier. A total of six areas were used to describe the fuel-air mixing concentration. A qualifier of 1 was given to the area if it appeared to contain any fuel, while an area was labeled 0 if it appeared to absent of fuel. Note that there was no attempt to designate differences in fuel concentration within an area or between areas. Areas were lettered 'A' through 'F' where 'A' was closest to the rotor apex and 'F' was located just above the injector hole. Figure 27 illustrates the segmented combustion chamber along with the multiple silhouettes of the rotor edge (designated as rotor advancement in figure). The multiple silhouettes of the rotor edge represent the rotor advancement between fuel-air concentration measurements.

For Case (i) and Case (ii), the observation time covers a period of 2.6 ms with five different intervals at 0.0, 0.8, 1.4, 2.0 and 2.6 ms. For Case (iii), the observation time lasted only 1.4 ms because of the late injection timing. A total of 10 injection events

were observed for each case. Once the areas were assigned a zero (0) or a one (1), the probability of finding fuel in each area at each observation time was calculated. Probabilities were calculated by taking the total fuel observations (intervals assigned 1) and dividing by ten (10). Results for this particular part of the study are discussed in a later section.

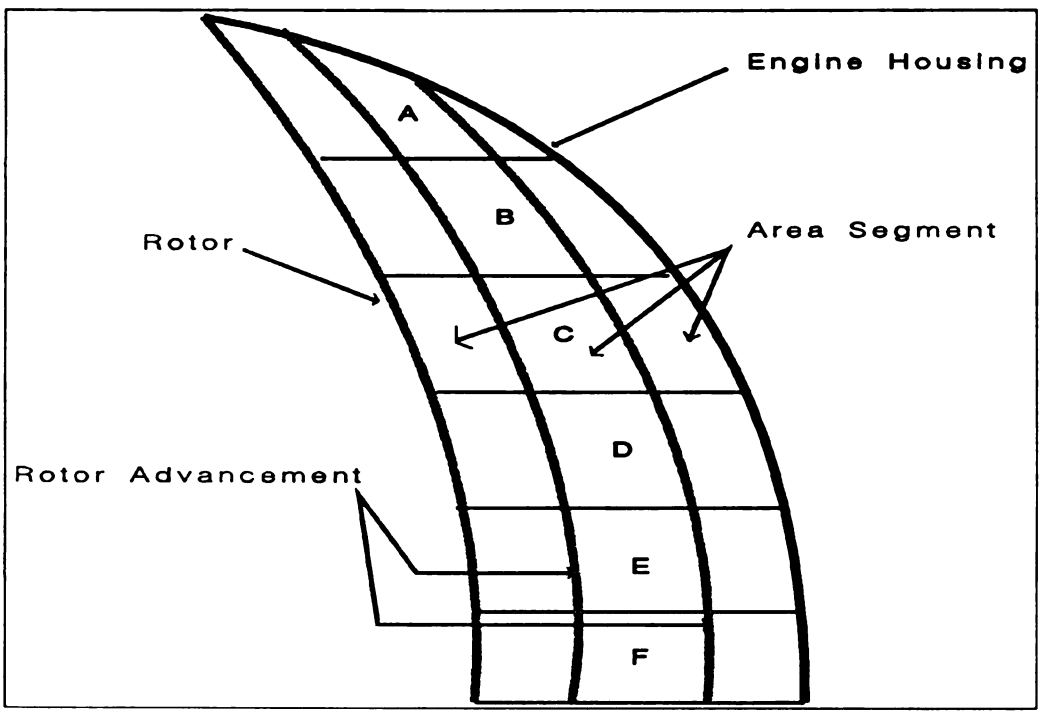

Figure 27 Segmented combustion chamber for observations of fuel-air mixing

CHAPTER 3

RESULTS AND DISCUSSION

3.1 Flow Visualization for Case (i)

In the following sections, the measured and analytical results for the case having an injection pressure of 70 MPa at a timing of 70° BTDC will be discussed.

3.1.1 Penetration Distances and Velocity Measurements

This section presents fuel spray characterization of kerosene fuel injected through a single hole nozzle having a L/D ratio equal to 4 and a spray orifice diameter of 0.217 mm. Fuel was injected into the combustion chamber toward the end of the compression stroke of a motored rotary engine at a crankshaft speed of 2000 rpm. At this speed, the crank shaft and the rotor rotational velocities were approximately 12°/ms and 4°/ms.

The engine pressure at injection was approximately 0.3 MPa. Pressure traces with and without fuel injection are shown in Figures 28 and 29. Figure 28 shows a maximum pressure of 1.39 MPa that occurs at top-dead-center (TDC). The maximum pressure in Figure 29 is 1.31 MPa, which also occurred at TDC. It is noted that at the end of intake, the pressure was assumed to be atmospheric. The lower pressure observed in the case with fuel injection of the liquid kerosene by the hot air in the compression chamber. During the evaporation process, the combustion chamber temperature was reduced. This also facilitated a drop in pressure within the chamber.

For case (i), the injection delay time was approximately 2.2 ms [25]. Using this 2.2 ms injection delay, a crank offset angle of 8.8° was used. The offset angle describes the compensation (in degrees) used to account for the injection delay time. The offset angle sets the proper rotor position at the start of injection. The injection event was observed within a time interval of 1.6 ms, so that injection occurred during a rotor position of 70° to 64° BTDC. From prior calibration testing, the estimated mass of fuel introduced per injection was 18 mg per injection. At the start of injection, Figure 30a shows a cone shaped spray formed at the nozzle exit. Figures 30b and 29c show that as the fuel jet moved outward from the nozzle tip, the liquid core of the jet traveled a finite distance, called the break-up length, before dissipating. After reaching the break-up length, the spray tip penetration velocity rapidly decreases. This spray behavior is a

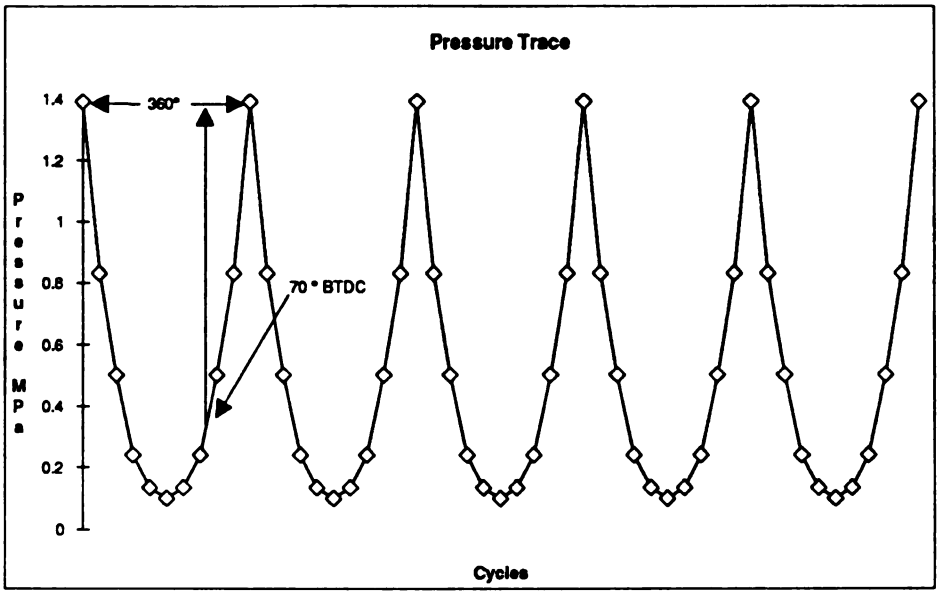

Figure 28 Pressure trace without fuel injection, engine speed of 2000 rpm

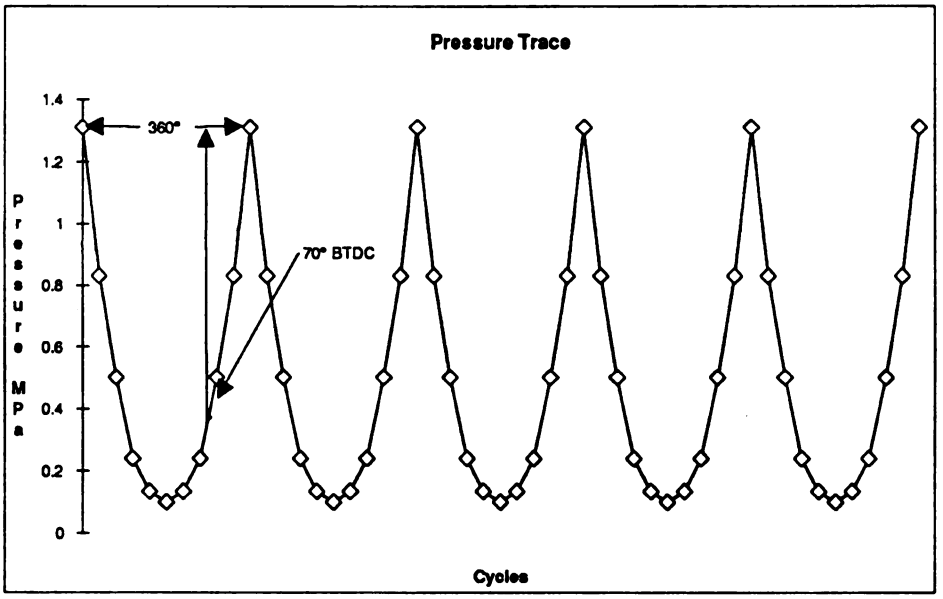

Figure 29 Pressure trace with fuel injection and engine speed of 2000 rpm

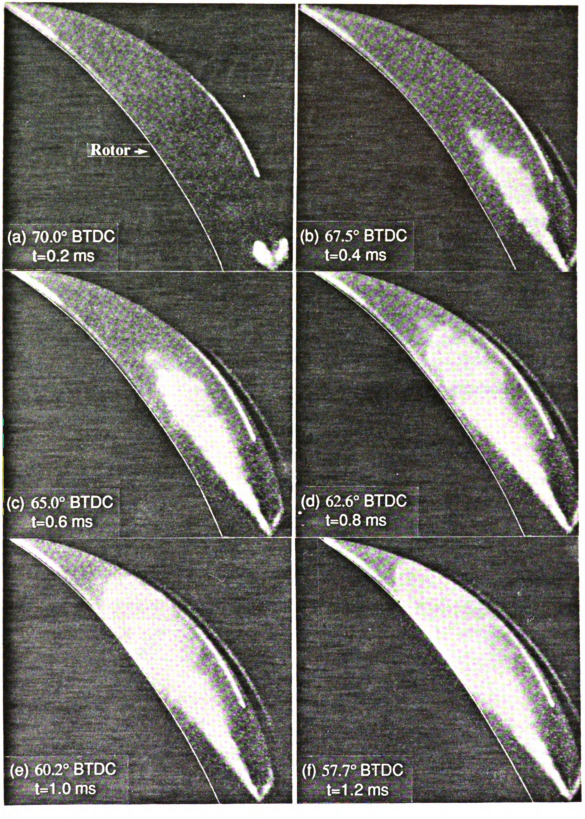

Figure 30 Successive frames of injection event at a pressure of 70 MPa

consequence of the aerodynamic resistance between the fuel and air charge in the combustion chamber, which usually leads to enhancement of the fuel-air mixing process. As the injection event proceeds, the fuel jet continues to penetrate the air charge, but at a much lower rate. At the outer surface of the jet, the mixing region grows in breadth, and the diameter of the liquid core will decrease in radius until it vanishes and the mixing region dominates the whole jet. Figures 30d-30f demonstrate these features of the fuel jet divergence and the significant decrease in velocity.

The penetration distances were measured and plotted for selected injection events using the high speed film of case (i) and can be seen in Figure 31. This figure illustrates typical penetration distances found in all injection events for this experiment. Notice that between 0.4 and 0.6 ms, the slopes of these curves suddenly decrease, quantifying the visual observation of liquid core break-up. At approximately 1.6 ms, the curves reach an asymptote of 100 mm. At this point, it was observed that the forward motion was negligible an no further measurements were taken. From Figure 30, a data spread of ± 20 mm in the penetration distance at 1.6 ms is observed. This was due to cyclic variations in the fuel injection system. The average penetration distances were also calculated for each time increment and are shown in this figure, as well as in Table 2.

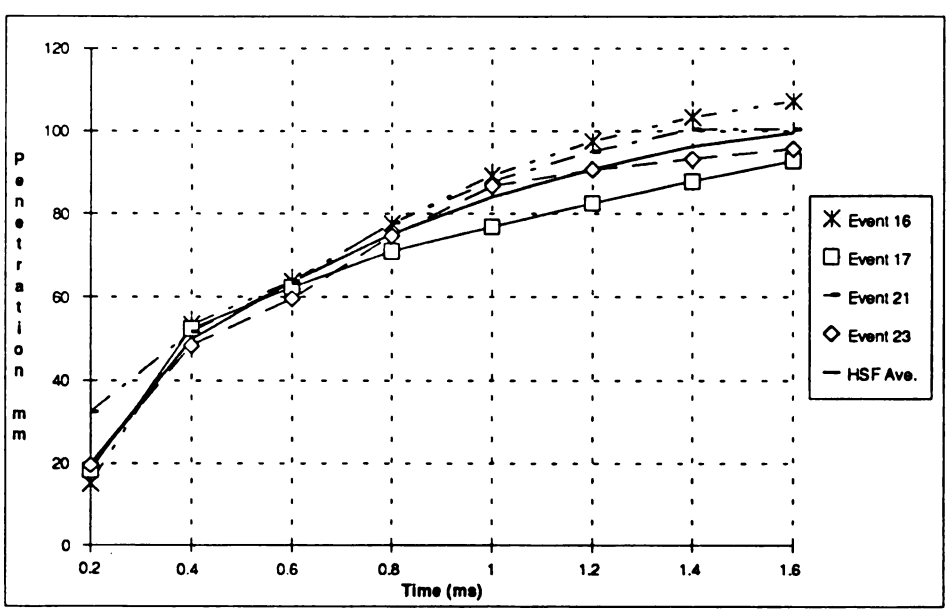

Figure 31 Penetration distance for selected events and event average

In Figure 32, the spray tip velocities for case (i) are shown. Figure 32 shows a maximum velocity of approximately 180 m/s for selected injection events at 0.4 ms (second frame of the capture event). All of the events shown in Figure 32 exhibit a

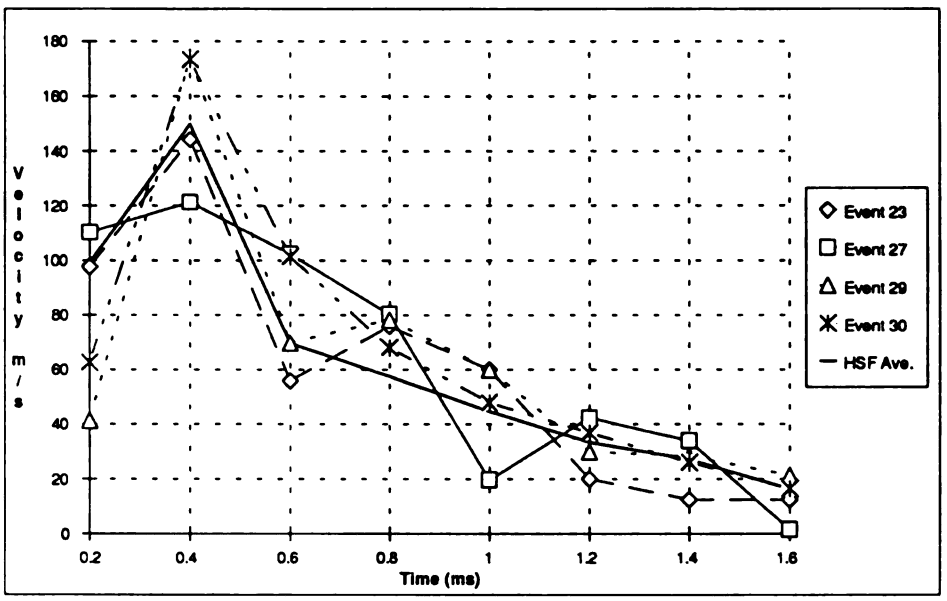

Figure 32 Velocity distribution for selected events and event average

Table 2 Penetration and spray tip velocity parameters for injection pressure of 70 MPa

Time (ms)	Penetration (mm)	Velocity (m/s)
0.2	19.8	98.9
0.4	49.8	150.0
0.6	63.7	69.7
0.8	75.2	57.3
1.0	84.1	44.7
1.2	90.8	33.4
1.4	96.2	27.3
1.6	99.5	16.4

decrease in the spray tip velocity after 0.6 ms which is a consequence of the liquid core break-up due to the aerodynamic interactions between the charge air and the fuel jet. The average initial spray tip velocity was calculated to be 98.9 m/s, followed by an average

penetration rate of 150 m/s at 0.4 ms after initial capture of the injection event. In addition to the curves in Figure 32, Table 2 provides the averaged spray tip velocities calculated at each time increment for a time span of 1.6 ms.

3.1.2 Calculated Penetration Distances for Case (i)

The quiescent air penetration distances were calculated for case (i) using equations (1), (2) and (3). Figure 33 compares calculated penetration distances with the average experimental values and the values for a single, typical injection event in the study. In the early stages of the injection process, there is fair agreement among the curves, particularly with respect to the shape of the curves. It is important to note that if the curves for the averaged and selected event were to be shifted to the left, excellent agreement with the calculated values would be achieved for the early stage of injection. This curve shifting is arguably correct in light of the cycle-to-cycle variability in the initiation of injection. Very few of the photographed injection events began exactly at the start of a film frame; rather, they began sometime during the interval before the frame

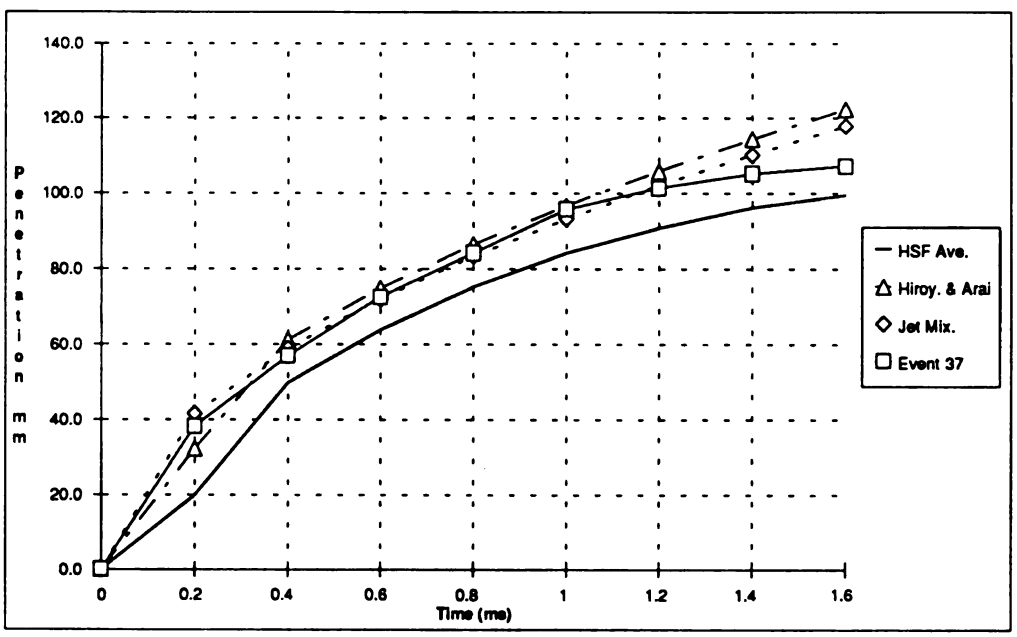

Figure 33 Penetration distances for experimental and calculated values

was exposed. At later stages in the event, starting around 0.4 to 0.6 ms, the shapes of the curves become much less similar. The quiescent curve appears to be a straight line, while the experimental curves of the present work become exponential and begin to approach an asymptote. This difference may well be explained by the fact that during the in-engine injection process, the air pressure within the combustion chamber increases, thus having a retarding effect on the forward momentum of the fuel spray. This pressure increase is not accounted for in the expressions of Hiroyasu and Arai [8] nor the jet mixing theory [27], so that penetration distances calculated by their expressions continues at the same slope. At the same time the pressure increases inside the chamber, the injection pressure is decreasing throughout the injection event. The resulting pressure term for both analytical expressions decreases in magnitude thus leading to smaller predicted penetration distances.

As a side note, the importance of cyclic variability in the injection process serves no other purpose than to detract from the engines performance. Watanabe and Hamai et al. [29] determined that the cyclic combustion variations in the rotary engine were significantly influenced by the geometric configuration and placement of the trailing side spark plug. Temperatures, mixture composition an gas velocities were considered in their study. In light of their findings that showed the variations in flame propagation going from the leading side spark plug to the trailing side spark plug led to combustion variations, the variations in the fuel-air mixing could possibly further enhance the combustion variations.

3.1.3 Calculated Spray Cone Angle for Case (i)

The calculated spray cone angles for case (i) were calculated using Equations (5) and (6) discussed in detail earlier in the thesis. The theoretical spray cone angle gave a result of 7.43° (included half angle). The second expression developed by Hiroyasu and Kadota [28] estimated the spray cone angle for an injection pressure of 70 MPa to be 16.1° This value was very close to the spray cone angle of the high speed film that was measured to be 16°± 1°. From these results, it can be seen that the expressions used to estimate the spray cone angle are quite good in their predictions for this study. Considering the theoretical expression and its result, 7.43° for the included half angle or 14.83° for the whole angle, its use can provide quick results at a slight expense of accuracy. Although the Hiroyasu and Kadota [28] expression is more demanding than the theoretical expression in its calculations, the results provided by Hiroyasu and Kadota [28] were much closer to the measured result in this case. It appears from these

observations that quick results for the spray cone angle can be found using the theoretical the jet mixing expression [27] but a more accurate result can be obtained with the quiescent expression of Hiroyasu and Kadota [28]. Simulation studies might utilize these analytical expressions for the spray angle in their code because of their relatively simple calculations and good results. In Table 3, the quiescent, theoretical and experimental averaged results for penetration distances, spray jet velocities and spray cone angles are given.

Table 3 Comparison of spray characteristics

	Penetration Distance (mm)		Penetration Velocity (m/s)		Spray Cone Angle
Time	0.4 ms	1.2 ms	0.4 ms	1.2 ms	-
Experiment Ave. (70MPa)	49.8	90.8	150.0	33.4	16°
Hiroyasu and Arai (70MPa)	61.2	105.9	145.0	46.0	-
Hiroyasu and Kadota (70MPa)	-	-	-	-	16.1°
Jet Mixing Theory (70MPa)	58.9	102.1	86.7	44.5	14.86°

3.1.4 Modified Penetration Distance Calculations

As mentioned before in section 3.1.3, the cycle-to-cycle variations in the fuel injection event appear to contribute to the deviations found between the experimental spray penetration distance results and the theoretical and quiescent results. Unlike the experimental results, the theoretical and quiescent calculations when plotted verses injection time did not appear approach an asymptote value. This characteristic of the calculated values was attributed to the pressure differential terms in the analytical expressions. The pressure terms were not assumed to vary with time in the original calculations. In an attempt to force the results form the analytical expressions toward a similar asymptote value found in the experimental results, the pressure terms were recalculated to account for the dynamic pressure change in the fuel injection event as well as in the compression process. New pressure terms were obtained by assuming three different scenarios: (1) assuming injection pressure to be constant while varying the chamber pressure over the compression cycle, (2) assuming both the injection pressure

and chamber pressure change during the compression cycle, and finally, (3) assuming that only the injection pressure changed during the cycle while holding the chamber pressure constant. While scenario (1) failed to provide any significant changes in the theoretical and quiescent penetration distances, scenario (2) and (3) showed significant decrease in the penetration distance. Results from the three scenarios indicate that the penetration distances that were analytically calculate were not greatly affected by the dynamic pressure change of the charged air in the compression chamber. When taken in combination, that is the dynamic pressure change in the charged air and the injection pressure change during the event, the penetration distance showed little difference from the scenario that considered only injection pressure changes.

In determining the pressure differential terms, assumptions concerning the engine pressure trace and the injection pressure trace were made. It was assumed that the engine pressure trace and injector trace were linear with crankshaft displacement during the injection event. Utilizing this assumption, it was a simple matter to calculate the pressure terms for the analytical expressions by subtracting the injection pressure by the chamber pressure at every 0.2 ms interval of the injection event. Linear interpolation was used to calculate the instantaneous pressure for both the engine and injector trace at each

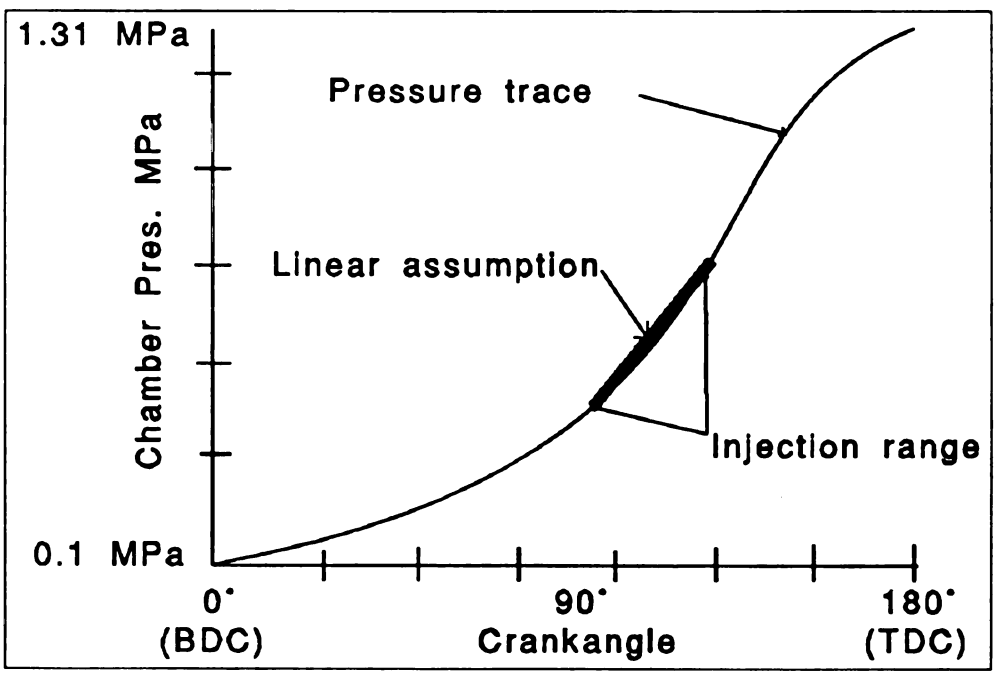

Figure 34 Linear assumption for chamber pressure

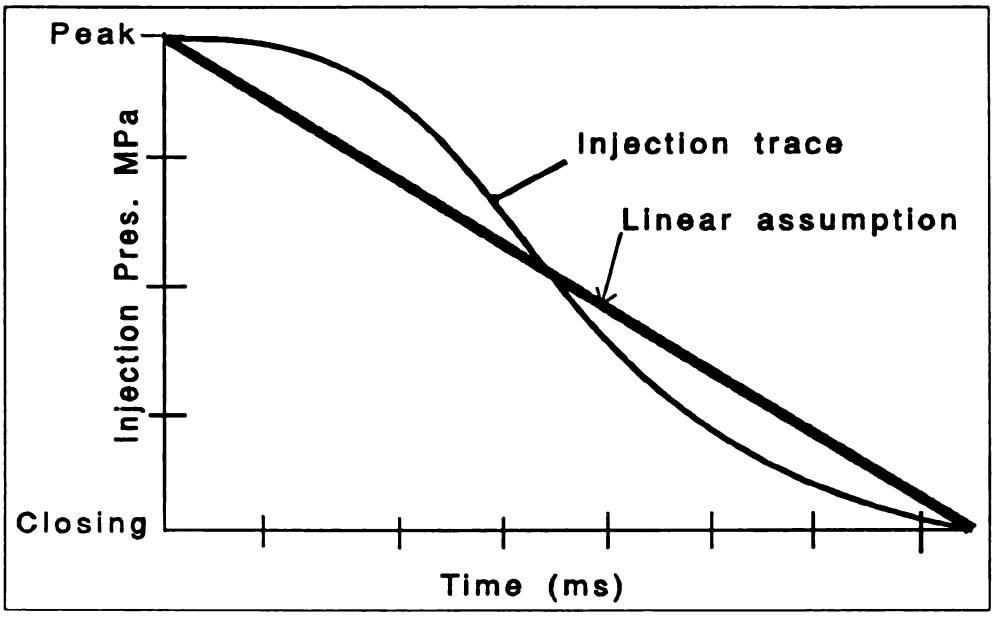

Figure 35 Linear assumption for the injection event

interval. The injection pressure was interpolated between the maximum injection pressure and the closing pressure of the nozzle spring that was indicated by a calibration reference manual [25]. The pressure trace interpolation used 90° BTDC and TDC as the end datum points. Though the accuracy of the pressure trace interpolation was questionable, especially at the extreme crank angles of the range, the penetration distance calculations were limited to ranges well within the end bounds. Figures 34 and 35 illustrate the linear assumptions made for the compression process in the engine and the injection event. These figures do not represent an exact replication of the actual traces and are only meant to illustrate the linear assumptions that were made.

In the final analysis, varying the pressure differential term throughout the injection event, as opposed to utilizing a constant, resulted in theoretical and quiescent responses that mirrored the averaged experimental penetration distance better. Other observations included that the engine pressure during the combustion cycle had little effect upon the penetration results. This observation indicated that the engine pressure calculations could be neglected without sacrifice to the penetration results. The approach toward an asymptotic value by the jet mixing [27] and Hiroyasu - Arai [8] values, which reflected the tendencies of the experimental results, occurred when scenario (3) was used. Table 4 presents the results of the Hiroyasu - Arai [8] penetration distances using the three scenarios.

Table 4 Modified penetration distances: Hiroyasu & Arai Expression

Time	Scenario 1		Scenario 2		Scenario 3		Original	
(ms)	ΔP^1	Dist.	ΔP^2	Dist.	ΔP^3	Dist.	ΔP	Dist.
----------	MPa	mm	MPa	mm	MPa	mm	MPa	mm
0.0	--	0.0	--	0.0	--	0.0	--	0.0
0.2	69.6	32.2	66.4	31.4	66.4	31.4	69.6	32.2
0.4	69.56	61.2	62.8	59.5	62.9	59.5	69.6	61.2
0.6	69.53	74.9	59.3	71.8	59.4	71.9	69.6	74.9
0.8	69.5	86.5	55.9	81.8	56.0	81.8	69.6	86.5
1.0	69.47	96.7	52.4	89.9	52.5	90.0	69.6	96.6
1.2	69.44	105.9	48.9	96.8	49.1	96.9	69.6	105.9
1.4	69.4	114.4	45.3	102.6	45.5	102.7	69.6	114.4
1.6	69.36	122.2	41.9	107.6	42.1	107.7	69.6	122.4

Table 5 Modified penetration distances: jet mixing expression

Time	Scenario 1		Scenario 2		Scenario 3		Original	
(ms)	ΔP^1	Dist.	ΔP^2	Dist.	ΔP^3	Dist.	ΔP	Dist.
----------	MPa	mm	MPa	mm	MPa	mm	MPa	mm
0.0	--	0.0	--	0.0	--	0.0	--	0.0
0.2	69.6	41.6	66.4	41.1	66.4	41.1	69.6	41.6
0.4	69.56	58.9	62.8	57.3	62.9	57.4	69.6	58.9
0.6	69.53	72.1	59.3	69.2	59.4	69.3	69.6	72.1
0.8	69.5	83.3	55.9	78.8	56.0	78.8	69.6	83.3
1.0	69.47	93.1	52.4	86.7	52.5	86.7	69.6	93.2
1.2	69.44	102.0	48.9	93.3	49.1	93.4	69.6	102.1
1.4	69.4	110.1	45.3	98.9	45.5	99.0	69.6	110.2
1.6	69.36	117.7	41.9	103.7	42.1	103.8	69.6	117.9

In Table 4, results show that the injection pressure dominates the chamber pressure term and has significantly more effect on the penetration distance. Table 5 contains the results of the jet mixing penetration distances [27] for the three scenarios. The terms ΔP^1 , ΔP^2 and ΔP^3 are the pressure differential terms for the three scenarios.

In Figure 36, the original and third scenario penetration distances are plotted for the theoretical and quiescent expressions. The experimental average is also plotted in Figure 36 and is labeled as HSF Ave. From the plot, it can be seen that the modified expressions track the experimental average very well. As the graph indicates, the consideration of dynamic pressure changes can enhance the predictive power of the analytical models for the penetration distance.

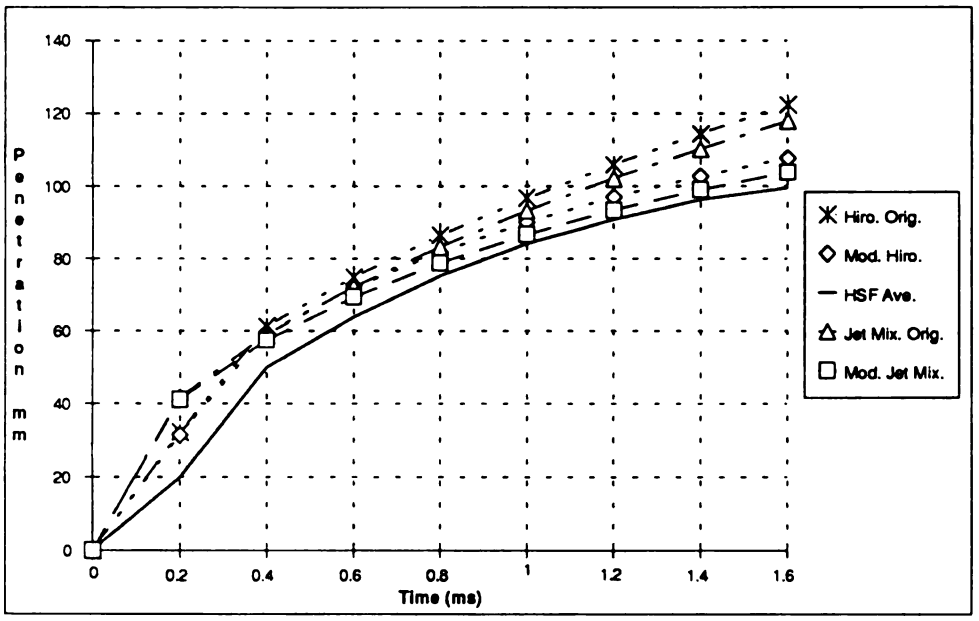

Figure 36 Penetration distances for standard and modified expressions

Velocities calculated from the original and modified penetration expressions provide more insight on the expressions ability to accurately predict the penetration distances. Figure 37 exhibits the velocities. Figure 37 contains plots of the velocities calculated from the penetration distances for both the original and modified version of the analytical expression. The average velocity for all the events is also shown in Figure37. Both velocities for the original and modified version of the Hiroyasu and Arai [8] track one another very closely through 0.6 ms. The velocities for the jet mixing

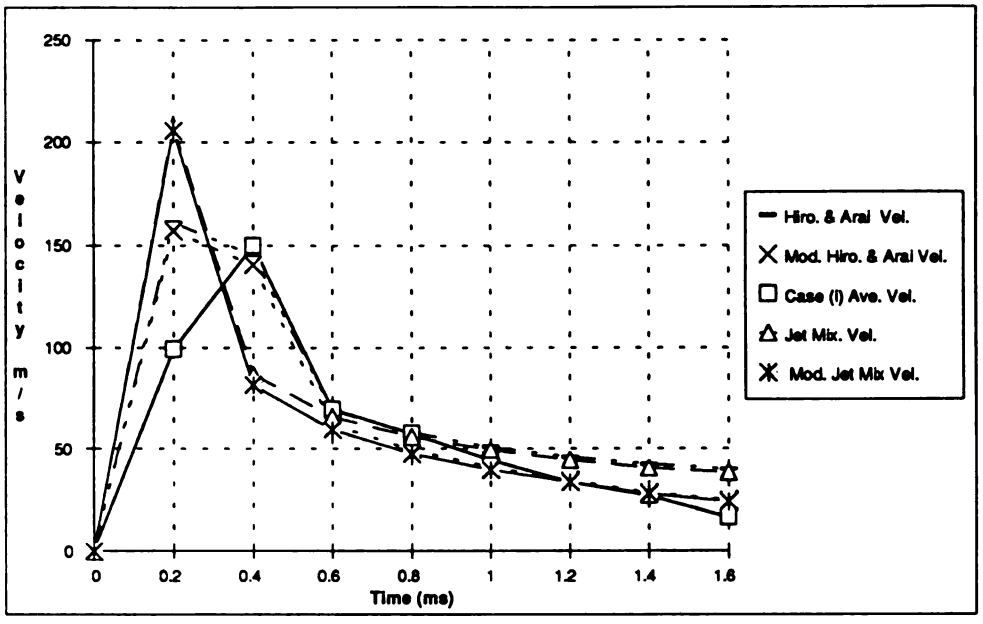

Figure 37 Velocity comparisons of original and modified expressions

expression are also very similar to one another during the first 0.6 ms. After 0.6 ms, the modified versions of the analytical expressions begin to follow the same paths and begin to deviate from the original velocities. Between 0.6 and 1.4 ms, the modified velocities are very close to the averaged velocities. The original versions of the analytical expressions never fall below 40 m/s. The final velocity calculated for the averaged velocity for the experiment was approximately 16 m/s, far below the original predicted velocity by the analytical expressions. The modified expressions however, predict the final velocity to be approximately 25 m/s. The modified velocities are still higher than the actual experimental velocity, but are close to the predictions of the original expressions.

3.1.5 Quantifying The Fuel-Air Mixture After Injection

The ability to characterize the fuel-air mixture in the combustion chamber before ignition plays an important role in the physical designs of the combustion chamber and the fuel delivery system. Ikegami et al. [30] studied the effects of combustion chamber shape and the role of pressurized injection in diesel engines. In their study, it was

determined that a combination of proper injection design and good chamber geometry enhances the mixing process. In this study, a simplistic approach was taken to quantify the fuel-air mixture in the combustion chamber at the end of the injection process.

The instant the fuel injection event terminated, the combustion chamber was sectioned into six distinct areas. Figure 38a-38e illustrate the sectioning technique applied. Each photo in Figure 38 represents one measuring time interval. The time intervals for case (i) were taken every 0.6 ms, over a time span of 2.6 ms. From the photos in Figure 38, it is observed that some areas are apparently free of fuel (lean), while other areas tend to contain the fuel (rich). In Figure 38a, fuel is found in area 'A', 'B', 'C', 'D', 'E' and 'F'. This photograph represents the instant after injection had terminated. Figure 38b shows the fuel distribution 0.8 ms after the injection termination and again, all areas appear to contain some fuel. After 1.4 ms, Figure 38c contains observable fuel in areas 'A' - 'E'; however, area 'F' is absent of fuel. The observations taken from the photo in Figure 38c indicate that the forward momentum of the fuel carries it away from the injector tip and out of the immediate area where the spark ignition occurs. Figure 38d has a similar distribution that was found in Figure 38c after 2.0 ms. Finally, after 2.6 ms, Figure 38e shows that in areas 'A' - 'C' and possibly 'D' there exists some fuel, while areas 'E' and 'F' are still empty of fuel.

Quantifying the fuel-air mixture in great detail was not the goal of this study. By labeling the sectioned area with a 1 if it contained fuel or with a 0 if no fuel was observed, simple probabilities of fuel existence within the area was possible. The probability distribution for finding fuel within an area is presented in tabular form in Table 6. Recent studies by Shimada [15] have shown that shadowed photography can provide insight on the evaporation of fuel into the charged air that direct photography may not provide. The question of considering the vaporized fuel and its possible contribution to the 'lean - rich' description of the fuel-air mixture can not be completely answered by this study. It is safe to assume that vaporization of the fuel does occur during and after injection and that higher probabilities of finding fuel (liquid or vapor) in an area would increase if vaporization can be included.

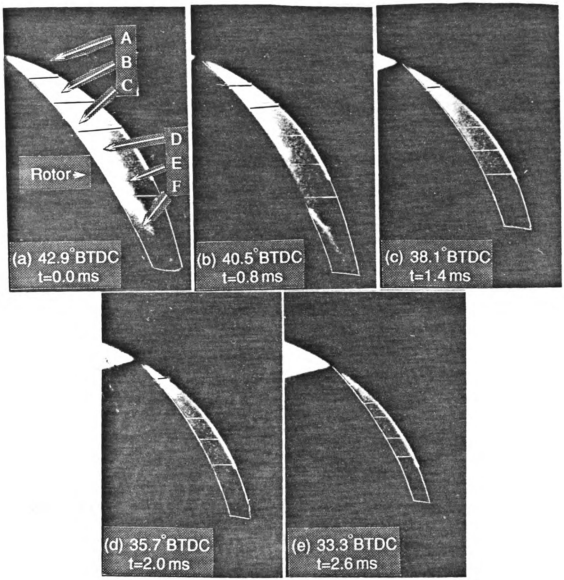

Figure 38 Fuel-air mixing after injection for Case (i)

Table 6 Probability of observing liquid fuel in segmented areas

Time (ms)	A	B	C	D	E	F
0.0	1	1	1	1	1	1
0.8	1	1	1	1	1	0.7
1.4	1	1	1	1	0.3	0
2.0	1	1	1	1	0	0
2.6	0.5	1	1	1	0	0

Area 'A' in Table 6 shows the presence of fuel at every point in the observation period except for the last observation time where fuel is found half the time. Areas 'B' - 'D' contain fuel throughout the observation period. The areas closest to the injector tip , 'E' and 'F' have fuel at most the first 2.0 ms after injection. For area 'E', the probability of having fuel is only 0.3 at 1.4 ms and 0.1 at 2.0 ms. In area 'F' , the probability of fuel existing has a 70% chance. It can be concluded from the observations of the last areas that the forward momentum carried most of the fuel into farther segments.

3.2 Flow Visualization for Case (ii)

Experimental measurements and analytical predictions are discussed in the following subsections. Case (ii) had a timing of 65° BTDC and an injection pressure of 44 MPa.

3.2.1 Penetration Distances and Velocity Measurements

For this section, all the engine operating parameters remained the same as in Case (i). The injection pressure and injection timing were adjusted however. The estimated amount of fuel introduced into the combustion chamber was approximately 10 mg per injection. The average duration time of injection was 1.2 ms. The injection delay time was determined to be 2.8 ms [25]. Using this delay time, a 11° angle off-set was established.

Figure 39 presents the fuel spray development for Case (ii). In this figure, the spray development process of the fuel jet is analogous to those described in Case (i). The fuel in Figure 39 makes contact with the rotor pocket before it reaches the engine housing which constrains the fuel to flow tangentially along the rotor surface as shown in

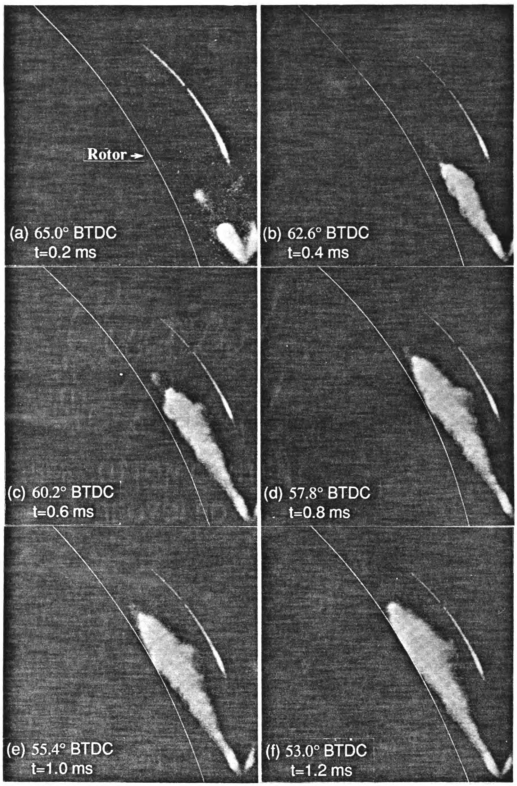

Figure 39 Successive frames of injection event at a pressure of 44 MPa

Figures 39a-39f. Figure 39 also shows that the penetration distance and the spray cone angle are dependent upon the injection pressure, which in turn affects the rate of air entrainment into the spray. These physical aspects are all related to the aerodynamic interaction at the liquid/gas interface.

Penetration distances were also calculated for the Case (ii). Figure 40 shows the penetration distance curves. these results are analogous to the penetration curve characteristics for Case (i) mentioned earlier. The plots for the penetration distances encompass the entire injection event unlike the plots for Case (i). Each curve has an initial positive penetration slope, followed by successive decreasing positive slopes. For Case (ii), the sudden change in the slopes that occur between 0.4 and 0.6 ms indicate liquid core break-up. This decrease in the break-up time is to be expected; at 44 MPa, the liquid core will have less momentum than at 70 MPa, and dissipation of this momentum by the charged air will take less time. All the curves in Figure 40 asymptotically approach a penetration value between 65 mm and 75 mm. The average penetration distance at each time increment over a 1.2 ms period can also be found in Table 7. Unlike the first case in this study which had an observation range over 1.6 ms, the observation range for this case lasted only 1.2 ms for two reasons. First, the injection event lasted for only 1.2 ms. Second, the forward momentum after 1.2 ms was barely measurable by visual means.

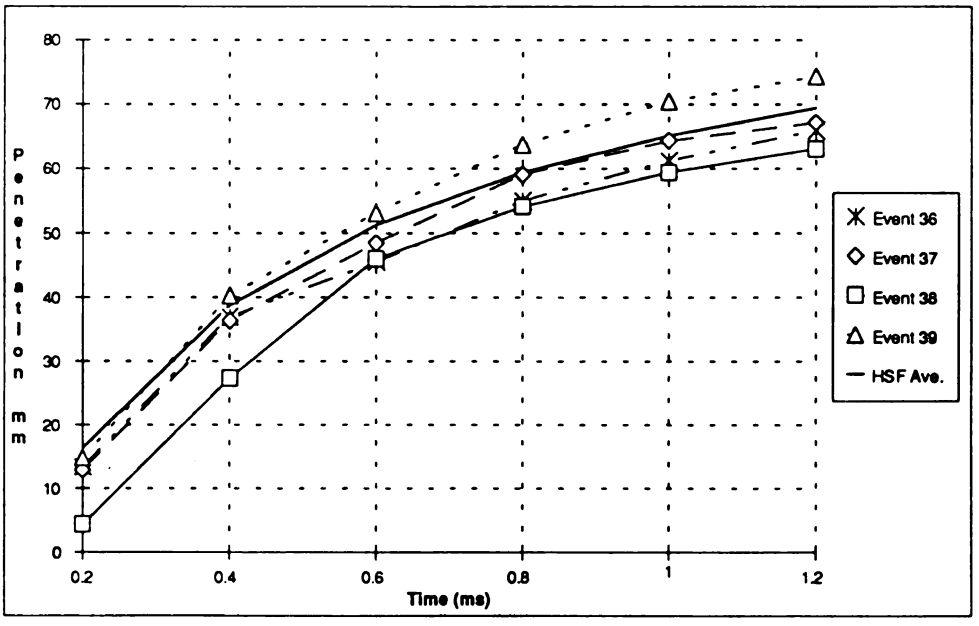

Figure 40 Penetration distances of selected events

Figure 41 presents the spray tip velocity of selected injection events for Case (ii). In Figure 41, all the injection events show an increase in velocity between 0.2 ms and 0.4 ms. After 0.4 ms, all events exhibit the same characteristics of a deceleration pattern that is sustained through the end of the injection event. At the lower injection pressures, there are corresponding lower spray tip velocities. The average velocity over 1.2 ms was calculated to be 57.9 m/s. The initial velocity was estimated to be 81.8 m/s, followed by an average velocity of 111.8 m/s at 0.4 ms. Table 7 lists the averaged spray tip velocities at each time increment for a time span of 1.2 ms.

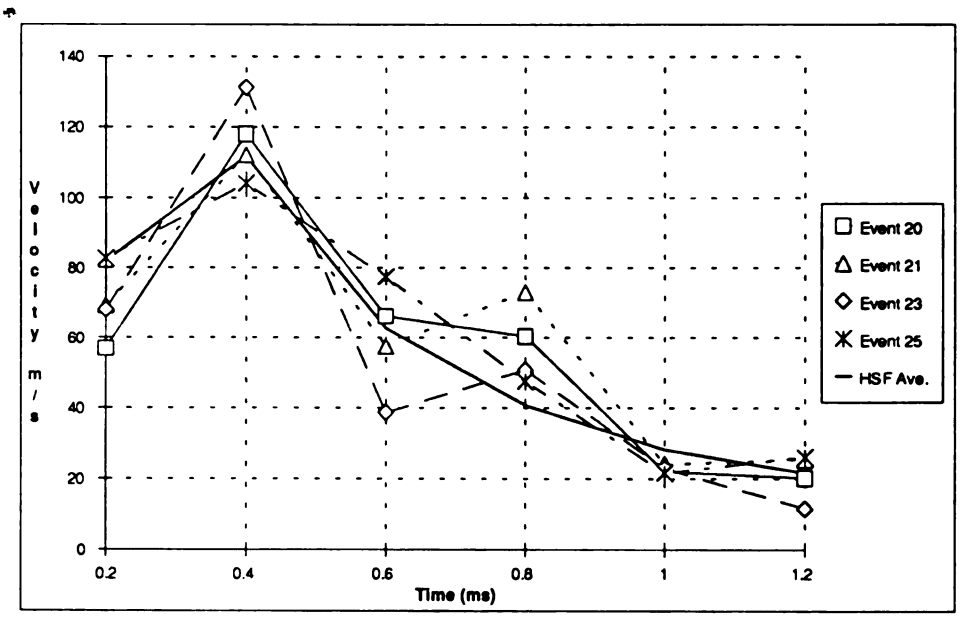

Figure 41 Spray tip velocities of selected events

Table 7 Penetration and spray tip velocity parameters for injection pressure of 44 MPa

Time (ms)	Penetration (mm)	Velocity (m/s)
0.2	16.4	81.8
0.4	38.7	111.8
0.6	51.3	62.7
0.8	59.4	40.8
1.0	65.1	28.3
1.2	69.4	21.7

3.2.2 Calculated Penetration Distances for Case (ii)

The quiescent air penetration distances were calculated again using equations (1), (2) and (3). The results of the calculations are very similar to the findings in Case (i). Figure 42 presents the penetration distances for the analytical expression, the average of all the events and a single typical event. In the early stages of the injection process, there is some agreement between the typical event and the expressions. The average of all the events is smaller in magnitude throughout the whole observation period. Again it is felt that the discrepancies between the averaged penetration distance and the other values are heavily influenced by the cyclic variations in the injection process. The analytical expressions contain two distinct slopes during the 1.2 ms. The first slope is contained in the first 0.4 ms. The penetration slopes and values of both the Hiroyasu-Arai [8] and the jet mixing theory [27] are almost identical over the entire range. Again as in Case (i), the penetration values of the two expressions do not appear to approach an asymptote. The penetration values obtained from the high speed film do however show effects of the increase in chamber pressure, and do gravitate towards a possible asymptote.

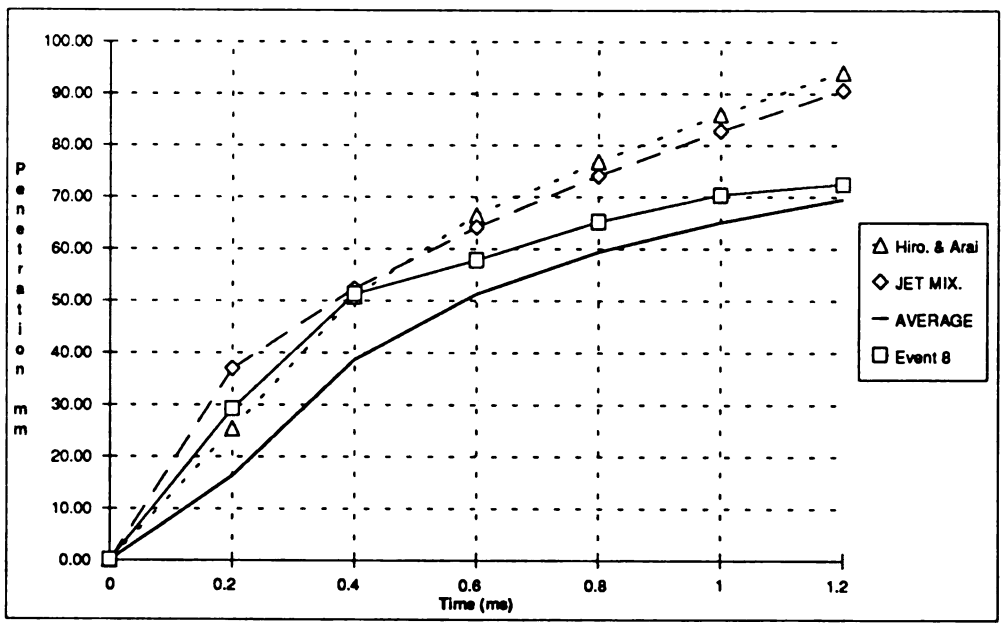

Figure 42 Penetration distances at an injection pressure of 44 MPa

3.2.3 Calculated Spray Cone Angle for Case (ii)

Using Equations (5) and (6), the spray cone angles were calculated. The spray cone angles for this case were slightly smaller than those found in the previous case.

Table 8 Comparison of spray characteristics

	Penetration Distance (mm)		Penetration Velocity (m/s)		Spray Cone Angle
Time	0.4 ms	1.2 ms	0.4 ms	1.2 ms	
Experiment Ave. (44MPa)	38.7	69.4	111.8	33.4	15°
Hiroyasu and Arai (44MPa)	50.8	94.1	127.0	41.0	-
Hiroyasu and Kadota (44MPa)	-	-	-	-	14.3°
Jet Mixing Theory (44MPa)	52.3	90.6	76.5	39.5	14.86°

Table 8 contains a summary of the calculated spray cone angle results and also the penetration and velocity results. The results show that at lower injection pressures, the spray cone angle tends to decrease.

The jet mixing theory [27] produced the same result of 7.43° for the included half angle, or 14.86° for the whole angle. The results were exactly the same due to the dependance of the jet mixing equation on only the densities of the air and fuel. The density of air was assumed to be the same for both Case (i) and Case (ii) since both utilized the same compression ratio. The density of the fuel was assumed to be constant over the injection period.

3.2.4 Modified Penetration Distance Calculations

The dynamic pressure changes within the engine were again analyzed to determine their effect on the calculated penetration distances. Once again the three scenarios discussed in an earlier section were considered. In the first scenario, it was assumed that the chamber pressure varied with time only. In the second scenario, it was assumed both the chamber and injection pressure varied in time. Finally, in the last

scenario, only changes in the injection pressure were considered. It was not surprising to find that again as in Case (i), the calculated penetration distances did not respond to the small changes in the chamber pressure. Only when the fuel injection pressure changes were considered did the penetration curves react differently. The same procedure for determining the differential pressure term in Case (i) was implemented. Once again, when the pressure term in the Hiroyasu-Arai [8] and the jet mixing expression [27] was varied as a function of the injection pressure, the resulting penetration curves flattened significantly. Even with the modified pressure term however, the curves failed to reach the average penetration curve of the high speed film as seen in Figure 43. After 0.4 ms, the modified curves have nearly the same slope as the averaged curve. From 0.0 ms to 0.4 ms, the modified curves penetrate farther into the compression chamber in the same amount of time as the averaged curve.

As in Case (i), the question that remains to be answered is how well can the modified expression predict the penetration of the fuel. It appears that the general shape of the modified penetration curves mirrors the averaged penetration curve very closely. This observation begs another question of how the possible effect of cyclic variation in

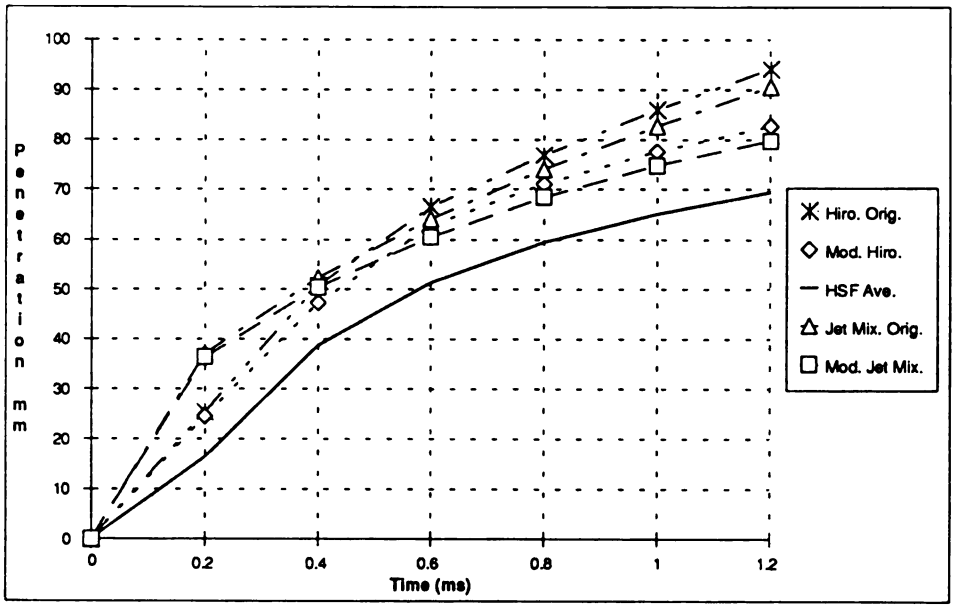

Figure 43 Penetration distances for standard and modified expressions

the fuel injector response might result in conservative film measurements. It has not been shown in this study that cyclic variation of the fuel injection event are significant enough to pull down the penetration curve observed in the 0.0 to 0.4 ms range. It is quite possible that the analytical expressions (original and modified) are over zealous in their predictions. The fact that the modified curves and the averaged curve cover approximately the same amount of distance between 0.2 ms and 1.2 ms tends to suggest to this author that cyclic variations are the greatest cause in the discrepancies found between the modified analytical and film penetration results. Tables 9 and 10 contain the results of the three scenario for both the Hiroyasu-Arai [8] and the jet mixing theory [27].

Table 9 Modified penetration distances: Hiroyasu & Arai Expression

Time	Scenario 1		Scenario 2		Scenario 3		Original	
(ms)	ΔP^1	Dist.	ΔP^2	Dist.	ΔP^3	Dist.	ΔP	Dist.
----------	MPa	mm	MPa	mm	MPa	mm	MPa	mm
0.0	--	0.0	--	0.0	--	0.0	--	0.0
0.2	43.6	25.3	40.5	24.5	40.5	24.5	43.6	25.4
0.4	43.57	50.7	37.6	47.2	37.6	47.2	43.6	50.8
0.6	43.54	66.4	34.67	62.8	34.7	62.8	43.6	66.5
0.8	43.51	76.7	31.74	71.0	31.8	71.0	43.6	76.8
1.0	43.48	85.7	28.81	77.4	28.9	77.5	43.6	85.9
1.2	43.45	93.9	25.87	82.6	26.0	82.7	43.6	94.1

Table 10 Modified penetration distances: jet mixing Expression

Time	Scenario 1		Scenario 2		Scenario 3		Original	
(ms)	ΔP^1	Dist.	ΔP^2	Dist.	ΔP^3	Dist.	ΔP	Dist.
----------	MPa	mm	MPa	mm	MPa	mm	MPa	mm
0.0	--	0.0	--	0.0	--	0.0	--	0.0
0.2	43.6	36.9	40.5	36.3	40.5	36.3	43.6	37.0
0.4	43.57	52.3	37.6	50.4	37.6	50.4	43.6	52.3
0.6	43.54	64.0	34.67	60.5	34.7	60.5	43.6	64.1
0.8	43.51	73.9	31.74	68.4	31.8	68.4	43.6	74.0
1.0	43.48	82.6	28.81	74.6	28.9	74.7	43.6	82.7
1.2	43.45	90.5	25.87	79.6	26.0	79.7	43.6	90.6

The results found in Tables 9 and 10 and observing their plots in Figure 43 implies that simulation programs might utilize the analytical expressions with some success when attempting to predict the penetration distances of fuel jet sprays.

As in Case (i), the determination of the velocities calculated from the original and modified penetration distances might provide more information about the ability of the expressions to accurately predict penetration distances. Favorable comparisons to the average velocity plot of the high speed film would indicate good predictive power. Figure 44 provides the velocity plots of the modified and original penetration expressions. Also included in Figure 44 is the average spray tip velocity measured from the high speed film. The original calculated velocities for the Hiroyasu-Arai [8] and the jet mixing [27] expression are very high when compared to the measured velocity at 0.2 ms. The original velocity and modified velocity for the Hiroyasu and Arai [8] track one another during the first 0.8 ms. This observation of tracking is also true for the jet mixing velocities. At 0.8 ms, the original and modified velocities for both expression separate where the original velocities assume a high prediction line while the modified velocities fall almost exactly on the average velocity line. At 1.2 ms, the original velocity lines have a value of approximately 40 m/s. The modified velocity curves have a value of

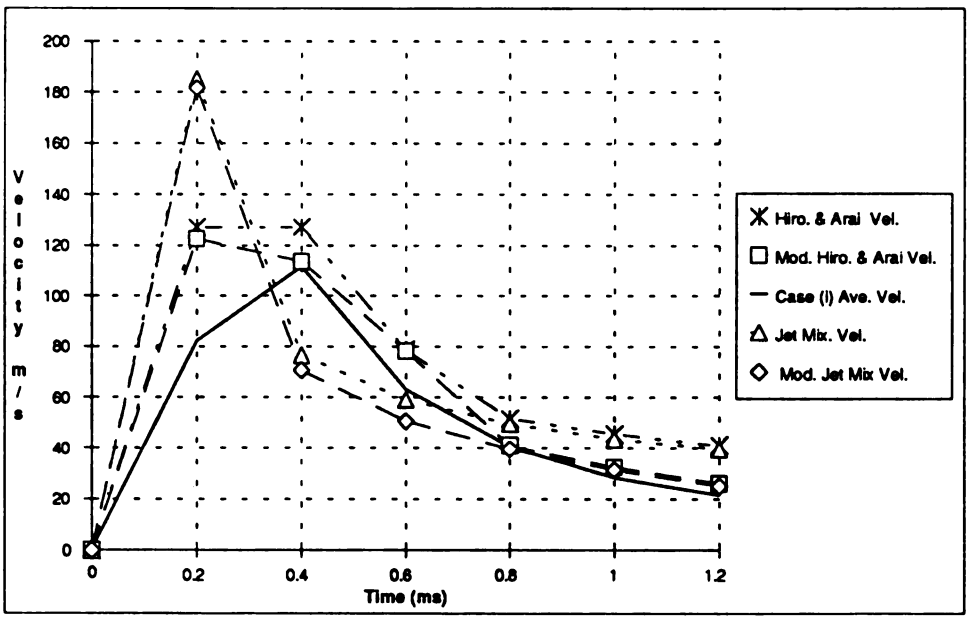

Figure 44 Velocity comparisons of original and modified expressions

25 m/s which is very near the average velocity of 20 m/s at 1.2 ms. These results indicate that the modified versions of the analytical expressions are better at predicting the penetrating distance than the original versions, especially well into the injection event.

3.2.5 Quantifying The Fuel-Air Mixture After Injection

The combustion chamber was again sectioned into 6 areas labeled 'A' - 'F'. Due to the later injection timing of 65° BTDC and a smaller injection pressure, the mixing results exhibit some slight differences from the observations in Case (i). Figure 45a-45f presents a typical mixing event observed in this case. Figure 45a contains fuel in all the area except 'A' at the instant the injection event terminated. In Figure 45b, 0.8 ms after termination, area 'E' is the only segment without fuel. A combination of the fuels forward momentum and the rotor advancement which decreases the area of observation explains the emergence of fuel in area 'A'. At 1.4 ms, the fuel appears to moved out of the two areas closest to the injector tip and is concentrated in areas 'A' - 'D' which can be observed in Figure 45c. Further investigation of the mixing process shows little difference from what was observed at 1.4 ms. Figure 45d shows that most of the fuel is concentrated in areas 'B' - 'C'. Fuel is observable in areas 'A' and 'D', but the fuel-air mixture is much leaner in these areas. Figure 45e shows much of the same results as Figure 45d, but also might show some fuel in are 'E'.

The results presented in this section are based solely on the observations obtained from the high speed film and the 35 mm photos of selected frames. The granular resolution of the high speed film was transferred to the 35 mm stills which made the identification of areas with a lean mixture was very difficult. Table 11 presents the probability of finding fuel in each area during each time interval.

Table 11 Probability of observing liquid fuel in segmented areas

Time (ms)	A	B	C	D	E	F
0.0	0	1	1	1	1	1
0.8	0.6	1	1	1	1	0.9
1.4	0.9	1	1	1	0.3	0.2
2.0	1	1	1	1	0	0
2.6	1	1	1	0.8	0	0

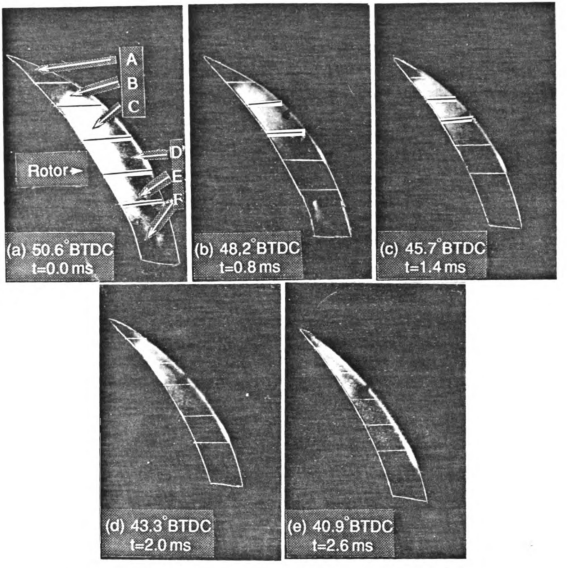

Figure 45 Fuel-air mixing after injection for Case (ii)

The probability of finding fuel in area 'A' increases as time increases. Forward momentum of the fuel along with the decrease in volume due to compression would explain this distribution for area 'A'. Typically, the middle areas 'B' - 'D' will contain fuel during the post-injection and pre-combustion period. The final two areas, 'E' and 'F' will contain some fuel during the first three observation stages, but forward momentum will ultimately carry the fuel out of the areas. By 0.2 ms into the observation period, area 'E' will only have a 30% chance of containing fuel, while area 'F' will contain fuel only about 20% of the time.

3.3 Flow Visualization for Case (iii)

Mixing observations are presented in the following subsections. Case (iii) has an injection pressure of 44 MPa and a timing of 55° BTDC

3.3.1 High Speed Film Observations

Figure 46 shows the fuel spray development for Case (iii). The early interaction of the fuel jet with the rotor surface, is indicated in Figures 46b-46e. Figures 46f-46i illustrate the deflection of the fuel jet from the rotor pocket toward the engine housing. The fuel-air mixing in his case was relatively weak as compared to the results in the prior cases. Due to the early interaction between the fuel spray and the rotor, no qualification of the spray characteristics were made other than the fuel-air mixing. One observation that can be made is the area that the jet consumes is much less than case (i) and (ii). This observation can be related to the physical amount of fuel introduced per injection is nearly half the mass seen in Case (i). In terms of Case (ii) which also injected at 44 MPa, the impingement on the rotor prohibits the spreading of the jet during the injection process. As seen in the velocity plots for the first two cases, higher injection pressures lead to higher spray tip velocities. Higher velocities have greater shear forces at the radial edge of the liquid core which results in a greater removal rate of liquid droplets from the liquid core at the radial edge. These observations would imply that the optimal fuel-air mixture is very likely to occur at high injection pressures within the combustion chamber.

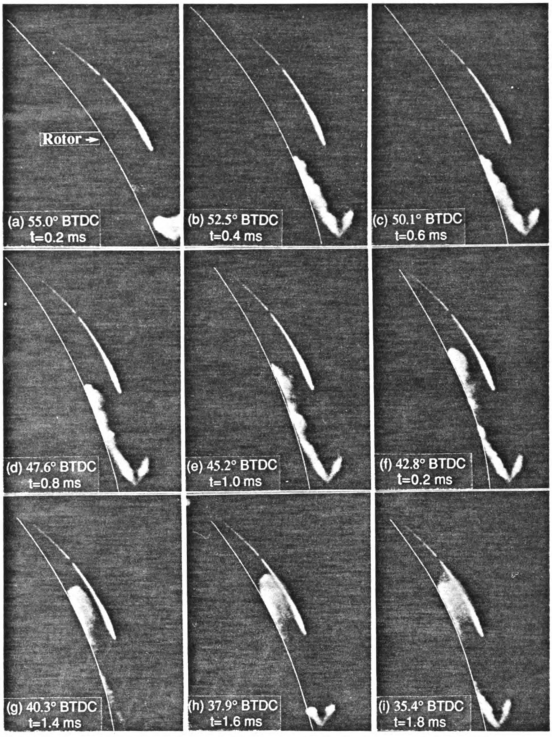

Figure 46 Successive frames of one injection event at a pressure of 44 MPa

3.3.2 Quantifying The Fuel-Air Mixture After Injection

Figure 47 illustrates the difficulties encountered when an attempt was made to quantify the mixing region. The observable volume was much smaller than those found in Case (i) and Case (ii). Figure 47a shows fuel existing in areas 'B', 'C' and 'D' at 0.0 ms after the injection event had ceased. At 0.8 ms, fuel can be found in areas B', 'C', 'D' and 'E' as shown in Figure 47b. The possibility of fuel existence in area 'A' might also be argued for due to the thin sheet of light near the apex. It determined that this flash in area 'A' could probably be attributed to light reflection at the Plexiglass window. The high speed film clearly indicates that the flash is a consequence of the laser light and plexiglass window interaction. In the process of transferring information from the high speed film to the 35 mm stills, the resolution of the small areas is not retained 100%. Figure 47c also produces the same results found in Figure 47b but also may include some fuel in 'F'. The observation range only contained three steps for this case due to the confined working volume. The probabilities of finding fuel in the six areas were again calculated from the data taken from the high speed film. Table 12 contains the probability results for this case.

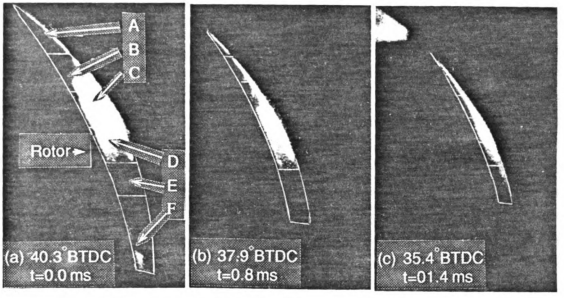

Figure 47 Mixing observations for Case (iii)

Table 12 Probability of observing liquid fuel in segmented areas

Time (ms)	A	B	C	D	E	F
0.0	0	1	1	1	0.1	0.5
0.8	0.1	1	1	1	0.3	0
1.4	0	0.9	1	1	0	0.1

From the table, it can be seen that there is not a high probability of finding fuel in area 'A' at any time. This indicates that the fuel impingement on the rotor which results in a severe forward momentum loss. The internal areas 'B', C' and 'D' almost always contain fuel throughout the observation period. It is in these areas that the fuel appears to be most concentrated. The two areas closest to the injector tip, 'E' and 'F' contain fuel only 10% to 50% of the time after the injection event has terminated.

3.4 Comparing Case (i) and Case(ii) Spray Characteristics

The similarities and differences in the spray characteristics of the two cases will be addressed in this section. It has already been stated that the physical combustion chamber volume consumed by the fuel spray during the injection event appears to be greater in Case (i) as illustrated in Figures 30 and 39 of the previous two sections. This result is to be expected due to the greater amount of fuel being introduced in Case (i).

Overall, the penetration distance, spray tip velocity and the spray cone angle were smaller in magnitude in Case (ii) for all observations. Although there is a 5° difference in the injection timing (70° BTDC for Case (i) and 65° BTDC for Case (ii)), it very unlikely that the timing could cause these differences between the cases. To further this idea, the penetration distance calculated from the analytical expressions were clearly very responsive to injection pressure changes rather than the compression pressure changes within the chamber during the injection event. So it appears after analyzing both cases that not only does the injection pressure play an important role in the fuel spray characteristics during the injection event, it also has a global effect upon the spray characteristics from event to event. Table 13 contains the penetration distances for both cases.

Table 13 Comparing penetration distances for Case (i) and Case (ii)

	Hiroyasu & Arai (mm)		Jet Mixing (mm)		Experimental Ave. (mm)	
Time ms	Case (i)	Case (ii)	Case (i)	Case (ii)	Case (i)	Case (ii)
0.0	0.0	0.0	0.0	0.0	0.0	0.0
0.2	31.4	24.5	41.1	36.3	19.8	16.4
0.4	59.5	47.2	57.4	50.4	49.8	38.7
0.6	71.9	62.8	69.3	60.5	63.7	51.3
0.8	81.8	71.0	78.8	68.4	75.2	59.4
1.0	90.0	77.5	86.7	74.7	84.1	65.1
1.2	96.9	82.7	93.4	79.7	90.8	69.4
1.4	102.7	-	99.0	-	96.2	-
1.6	107.7	-	103.8	-	99.5	-

From Table 13, it can be seen that the penetration distance decreases as the injection pressure decreases over the first 1.2 ms. The results for the Hiroyasu-Arai [8] and the jet mixing [27] expressions were obtained by assuming the pressure differential term fits the third scenario. The modified theoretical estimation does a better job of approximating the penetration distance for both cases. Figures 48 illustrate the penetration distances for both cases.

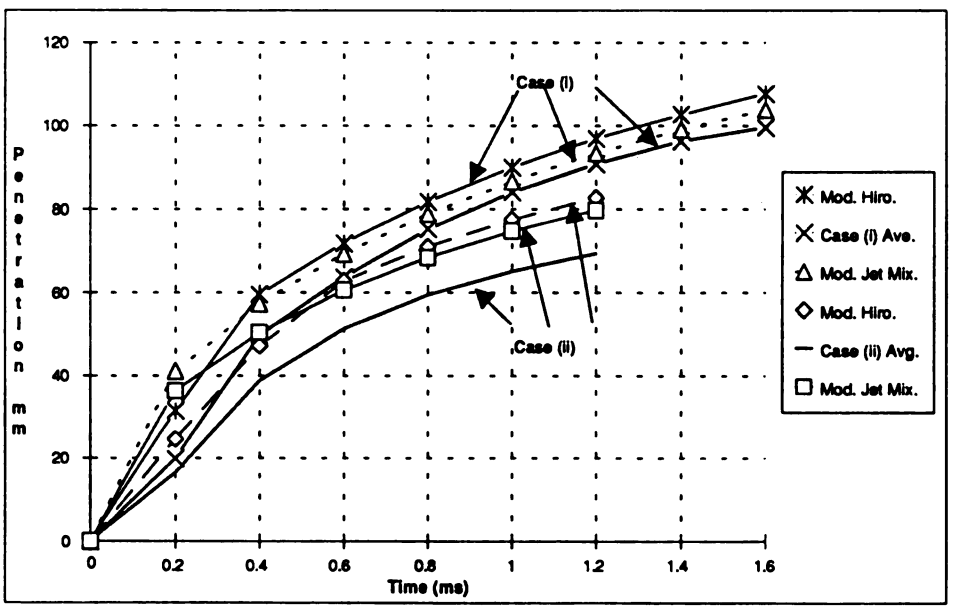

Figure 48 Penetration distances for both Case (i) and Case (ii)

Table 14 shows that the spray cone angle also decreases with a decrease in injection pressure.

Table 14 Spray cone angle comparison

	Hiroyasu & Kadota	Jet Mixing	Experiment
Case (i)	16.1°	14.86°	16.0°
Case (ii)	14.3°	14.86°	15.0°

3.5 Nozzle Tip Verification

The nozzle tip used throughout this study was part of a special set manufactured by BKM Inc. Orders were placed to have nozzle tips that re-directed the spray at orientations of 60°, 45° and 30° from the nozzle axis. Upon receiving these tips, it was necessary to observe the spray formations induced by these tips in order to verify their operational status. The first nozzle tested was the 60° tip. It proved to operate very successfully at all injection pressure loads. Figure 49 illustrates the jet formation of the

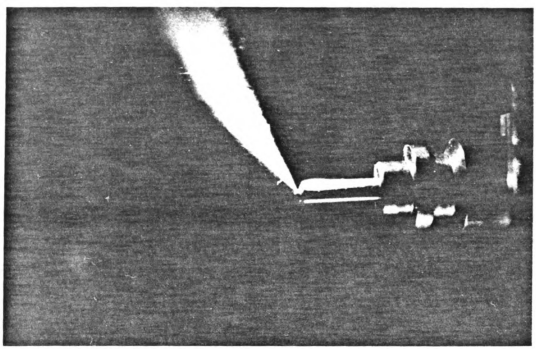

Figure 49 Injection into ambient conditions using 60° nozzle

60° nozzle fired into ambient conditions. The 45° tip was then tested with less than satisfying results. It appeared from the spray formulations captured on high speed 35 mm film that tip had a leaking problem. Large fuel droplets and inconsistent spray patterns were observed during the tips testing. Figure 50 shows a 45° injection event also conducted in ambient conditions. The slow exposer time tends to exaggerate the large fuel droplets that can be seen streaking away from the main jet formation; however, no events of the 60° test produced these same results. Previous studies have indicated that the nozzle hole shape has a great influence on the jet formation [31]. The nozzle hole geometry of this particular 45° tip could be the reason for its inconsistent performance. The 30° nozzle was not tested due to the fact that its angled injection would not lend itself to easy flow visualization studies in the motored engine. It was determined in the static test that at all injection timings would impinge on the rotor at a 30° angle of injection.

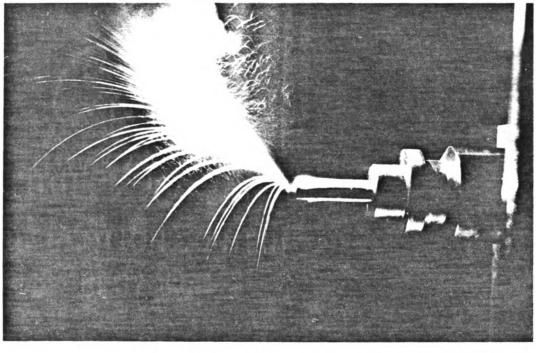

Figure 50 Injection into ambient conditions using 45° nozzle

3.6 Blowby Observations

Recent studies have determined that there is existence of blowby in the motored rotary engine without fuel injection. The blowby jet which is created when separation

between the apex and the engine housing occurs has been observed in high speed films and measured with Laser Dopler Velocity (LDV) techniques [1,32]. When observing the high speed films for each case, blowby can be seen during and after the fuel injection event. The airflow past the apex seal was seeded with the fuel particles from the fuel injection event; however, exactly how much influence did the injection event have on the blowby can not be said. Measuring the blowby during fuel injection with LDV techniques might provide some insight to the question of how the fuel injection effects the blowby in the engine. Figure 51 illustrates the blowby seen past the apex seal after an injection event.

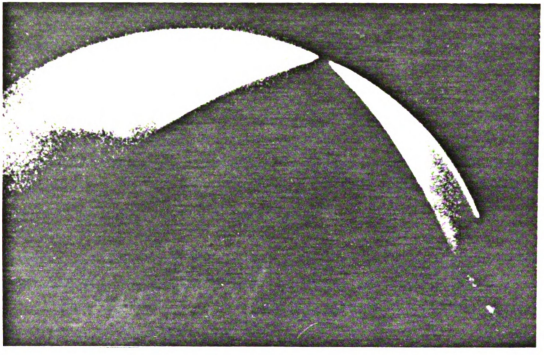

Figure 51 Blowby seen in the engine after the injection event

CHAPTER 4

SUMMARY AND CONCLUSIONS

Some characteristics of the behavior of a high pressure fuel injected into the combustion chamber of a rotary engine have been described by analyzing high speed films of the process. In addition to the qualitative description of the injection process, the films provide quantitative information such as spray tip penetration velocities and spray angles. Comparison with current fuel injection models gives additional insight on the characteristics of the fuel spray. The following remarks can be made:

1. Spray tip penetration distances and velocities are significantly influenced by injection pressure. Both increase with an increase in the injection pressure.

2. At these relatively high injection pressures (44 and 70 MPa), the combustion chamber air flow seems to have little influence on the spray characterization as confirmed by both visual observations and comparisons with quiescent air models. After the injection process is completed, the fuel-air distribution is significantly affected by the combustion chamber air flow.

3. The Hiroyasu and Arai [8] and the jet mixing [27] models describing spray characteristics for fuel injection into quiescent air can be used to predict injection penetration in simulation studies, provided the air pressure differential term in the expression is allowed to vary with time.

4. At higher injection pressures, the jet mixing area is larger due to the higher velocities and greater shear stresses at the radial edge of the liquid core. These higher velocities tend to enhance the break-up of the fuel spray.

5. Liquid core break-up length appears to increase with an increase in the injection pressure.

6. Late fuel injection at high pressures can lead to direct impingement of fuel on the rotor which results in a reduction of fuel-air mixing.

7. Experiments have shown the Hiroyasu and Kadota [28] spray cone angle expression to be very adequate at predicting spray cone angles while varying the injection pressure.

8. Pressure traces might be utilized in numerical simulations to calibrate evaporation rates during the injection process.

9. Inclusion of a pressure differential term in the quiescent Hiroyasu-Arai model [8] and the theoretical jet mixing equation [27] can provide better estimations of the fuel penetration distance.

10. For these experiments, it was observed that there existed areas of rich and lean fuel-air mixture.

11. Blowby can have a major influence on the local air-fuel ratio existing in the combustion chamber prior to ignition.

CHAPTER 5

RECOMMENDATIONS

The observations and ideas discussed in this study are not intended portray, nor do they approach a complete understanding of direct fuel injection within a rotary engine. Research is a continuous process that never stops. It is hoped that this study might provide some foundation for further work towards a better understanding of the combustion process in the rotary engine. Future work that might build upon the findings of this study will now be recommended.

1. It appears from the results in this study that analytical expressions might be used to predict penetration distances of the fuel spray with some success. Further investigations might reveal how the cyclic characteristics of the fuel injection system when captured on synchronized film lead to differences in the experimental and calculated results.

2. A complete mapping between the spray tip velocity and fuel injection pressure might be accomplished by using LDV techniques over a variety of operating ranges of the engine.

3. The mixing process within the combustion chamber after injection was briefly discussed in this study for all three cases. Future studies might concentrate on the mixing characteristic of the combustion chamber using other optical recording techniques that can access the close quarters of the combustion chamber. Improving the combustion process will clearly depend heavily upon the understanding of the mixing process.

4. The influence that the fuel injection has upon the leakage past the apex seals should be studied in order to accommodate its effects in simulation modeling of the rotary engine.

REFERENCES

LIST OF REFERENCES

1. Chouinard, E., "Experimental Investigation of the Flow Field in a Motored Rotary Engine Assembly," Thesis for the Degree of M.S. at Michigan State University, 1990.

2. Hamady, F.J., Kosterman, J., Chouinard, E., Somerton, C., Schock, H., Chun, K. and Hicks, Y., "Stratified Charge Rotary Engine Studies at the MSU Engine Research Laboratory," SAE Paper 890331. Also in SAE *Trans.*, Vol 98, Sec. 3, 1989.

3. Haddad, S.D., Advanced Diesel Engineering and Operation, Ellis Horwood Limited, New York, NY., 1988.

4. Savey, C.W., Beck, J.N., Dobovisek, Z. and Gevert, K., "Injection Characteristics of High Pressure Accumulator Type Injector," SAE Paper 890266, 1989.

5. Kato, T., Tsujimura, K., Shintani, M., Minami, T. and Yamaguchi, I., "Spray Characteristics and Combustion Improvement of D.I. Diesel Engine with High Pressure Fuel Injection," SAE Paper 890265, 1989.

6. Katsura, N., Saito, M., Senda, J. and Fujimoto, H., "Characteristics of a Diesel Spray Impinging on a Flat Wall," SAE Paper 890264, 1989.

7. Minami, T., Yamaguchi, I., Shintani, M., Tsujimura, K. and Suzuki, T., "Analysis of Fuel Spray Characteristics and Combustion Phenomena under High Pressure Fuel Injection," SAE Paper 900438, 1990.

8. Hiroyasu, H. and Arai, M., "Structures of Fuel Sprays in Diesel Engines," SAE Paper 900475, 1990.

9. Hiroyasu, H. and Nishida, K., "Fuel Spray Trajectory and dispersion in a D.I. Diesel Combustion Chamber," SAE Paper 890462, 1989.

10. Koo, J-Y. and Martin, J.K., "Droplet Sizes and Velocities in a Transient Diesel Fuel Spray," SAE Paper 900397, 1990.

11. Yoshikawa, S., Furusawa, R., Arai, M. and Hiroyasu, H., "Optimizing Spray Behavior to Improve Engine Performance and to Reduce Exhaust Emissions in a Small D.I. Diesel Engine," SAE Paper 890463, 1989.

12. Heinze, T. and Schmidt, T., "Fuel-Air Ratios in a Spray, Determined between Injection and Autoignition by Pulsed Spontaneous Raman Spectroscopy," SAE Paper 892102, 1989.

13. Arcoumanis, C., Cossali, E., Paal, G. and Whitelaw, J.H., "Transient characteristics of Multi-Hole Diesel Sprays," SAE Paper 900480, 1990.

14. Werlberger, P. and Cartellieri, W., "Fuel Injection and Combustion Phenomena in a High Speed DI Diesel Engine Observed by Means of Endoscopic High Speed Photography," SAE Paper 870097, 1987.

15. Shimada, T., Shoji, T. and Takeda, Y., "The Effect of Fuel Injection Pressure on Diesel Engine Performance," SAE Paper 891919, 1989.

16. Raju, M.S. and Willis, E.A., "Analysis of Rotary Combustion Processes Based on Unsteady, Three Dimensional Computations." AIAA-90-0643, 1990.

17. Raju, M.S. and Willis, E.A., "Computational Experience with a 3-D Rotary Engine combustion Model," presented at the 1990 Joint AIAA/FAA.

18. Abraham, J., Wey, M.J. and Bracco, F.V., "Pressure Non-Uniformity and Mixing Characteristics in Stratified-Charge rotary Engine combustion," SAE Paper 880624, 1988.

19. Abraham, J. and Bracco, F.V., "Comparisons of Computed and Measured Pressure in a Premixed Charge Natural Gas Fueled Rotary Engine," Rotary Engine Design: Analysis and Development, SAE SP-768, SAE, 1989, pp. 117-131.

20. Shih, T. I-P., Schock, H.J. and Ramos, J.I., "Fuel-Air Mixing and Combustion in a Two-Dimensional Wankel Engine," SAE Paper 870408, 1987.

21. Steinthorsson, E., Shih, T. I-P., Schock, H.J. and Stegeman, J., "Calculation of the Unsteady, Three-Dimensional Flow Field Inside a Motored Wankel Engine," SAE Paper 880625, 1988.

22. Li, T., Steinthorsson, E., Shih, T. I-P. and Nguyen, H.L., "Modeling and Simulation of Wankel Engine Flow Fields," SAE Paper 900029, 1990.

23. Hamady, H.J., Stuecken T. and Schock, H.J., "Airflow Visualization and LDA Measurements in a Motored Rotary Engine Assembly Part 1: Airflow Visualization," SAE Paper 900030, 1990. Also to appear in SAE *trans.*, 1990.

24. Mazda Motor Co., "Mazda RX-7 Workshop Manual," Repair Manual, 1984.

25. BKM, Inc., F-429, "Calibration Test Report Servojet Injector for NASA Lewis Research Center."

26. Lefebvre, A.H., 'Properties of Sprays," International Conferences on Mechanics of Two-Phase Flows, 1989.

27. Abramovich, G.N., Theory of Turbulent Jets, MIT Press, Cambridge, Mass., 1963.

28. Hiroyasu, H. and Kadota, T., "Fuel Droplet Size Distribution in a Diesel Combustion Chamber." SAE *trans.*, Paper 74017, 1974.

29. Watanabe, S. and Hamai, Y., "Investigation of Cyclic Combustion Variation in Rotary Engine," SAE Paper 890327, 1989.

30. Ikegami, M., Fukuda, M., Yshihara, Y. and Kaneko, J., "Combustion Chamber Shape and Pressurized Injection in High-Speed Direct-Injection Diesel Engines," SAE Paper 900440, 1990.

31. Ohrn, T.F., Senser, D.W. and Lefebvre, A.H., "Geometrical Effects on the Breakup of High-Velocity Jets," ASME Paper, Winter Anual Meeting, 1990.

32. Chouinard, E., Hamady, F.J. and Schock, H.J., "Airflow Visualization and LDA Measurements in a Motored Rotary Engine Assembly Part 2: LDA Measurements," SAE Paper 900031, 1990. Also to appear in SAE *trans.*, 1990.